8-25-2016

Wafer Level Characterization of Infrared Detectors

Teressa Rose Specht

Teressa Rose Specht
Candidate

Electrical and Computer Engineering
Department

This thesis is approved, and it is acceptable in quality and form for publication:

Approved by the Thesis Committee:

Dr. Sanjay Krishna , Chairperson

Dr. Ganesh Balakrishnan

Dr. Brianna Klein

Dr. Payman Zarkesh-Ha

WAFER LEVEL CHARACTERIZATION

OF INFRARED DETECTORS

by

TERESSA ROSE SPECHT

BACHELOR OF SCIENCE ELECTRICAL ENGINEERING
UNIVERSITY OF NEW MEXICO, 2012

THESIS

Submitted in Partial Fulfillment of the
Requirements for the Degree of

MASTER OF SCIENCE

ELECTRICAL ENGINEERING

The University of New Mexico
Albuquerque, New Mexico

July 2016

DEDICATION

To my family,

Your love, support, encouragement, and prayers

have inspired me to work hard all my life and achieve all that I have accomplished.

I love you and you will always inspire me to be the best person I can be.

To my faith in Jesus Christ,

with His grace and guidance I have found my calling to be an engineer.

"Science without religion is lame, religion without science is blind."

-Albert Einstein

ACKNOWLEDGEMENTS

First of all, I would like to thank my committee chair Dr. Sanjay Krishna for his patience and encouragement as he guided me throughout this process. I have come to realize that graduate research is a very rewarding experience and Dr. Krishna's counsel during my thesis work has helped me push through all the obstacles I faced. Sanjay, it is my pleasure to call you my mentor, colleague, confidant, and friend!

I would also like to thank my committee members Dr. Ganesh Balakrishna, Dr. Brianna Klein, and Dr. Payman Zarkesh-Ha for advising me through my research and thesis, but most importantly during my undergraduate and graduate studies. I have taken a total of 10 classes from my committee professors! You all have made a positive impact on my engineering career with your great teaching and mentorship. Your impact has influenced me to choose a path of optoelectronics and detectors, I am grateful to be a part of this fast-paced and exciting area of study.

Brianna, you in particular were with me in the trenches of this project and because of your positive attitude and daily help I was able to work through many challenges. I am so grateful you were there to listen to all of my complaints when the probe station broke or something went horribly wrong with my measurements. You would give me ideas to fix the probe station or look at my data to offer suggestions for measurement improvements. You also offered advice on any topic I came to you with, whether it is using cell phones to take MBE temperature measurements or where the best bike routes are in Albuquerque. You are such a giving person and I can't thank you enough for being an amazing soundboard, technical counsel, and friend.

To my graduate advisor Elmyra, thank you for being such a wonderful graduate advisor. You have been there for me even when I was in Colorado and couldn't visit your office. UNM and the ECE department are very lucky to have such a talented educator like you keeping us students in line.

I also want to thank and say "WHAT!!!" to my research group at CHTM as well as others that I have come to know at CHTM – Brianna, Lilian, Vinita, Marziyeh, Ali, Sadhvikas "Happy", Zahra, Ted, Clark, Sen, David R., Stephen, and the amazing staff who keep CHTM running as a successful research institution. You are all wonderful and brilliant people! I have enjoyed spending time, laughing and running with you, well some of you for that last one! I am grateful for all that you have taught me. I never really thought that graduate school was for me but you have certainly helped me understand why it is the most difficult yet rewarding academic experience in life!

I would like to acknowledge my family and friends who have been there for me. My aunts JoAnn, Gloria, and Bernadette; my uncles Eddie, Steve, Bob, Don, Carlos; my closest cousins Carmella, Rachael, Larry, Charlene, and Kevin; classmates and friends

Emma, Erum, Javad, Nadeem, Vijay, Zach, Kaiya, Karla, and bestie Kerianne. Your support and encouragement are worth more than words can say! I am very happy to have each of you in my life, no matter how big or small your role is, and I am glad to be a part of each of your lives. In particular, thank you Mike R. for keeping me company when I stayed late at the lab taking my temperature measurements. All those late nights and stressful days were more bearable with you there and for that I am grateful.

Lastly, I want to show my deepest gratitude to my mom Mabel, my dad Michael, my brother Mike and my sister Alyssa. Our family unit is remarkable, I could not do anything without your unfailing and unconditional love! There have been a lot of laughs, tears, smiles, hugs, and wonderful adventures as a family that I will always remember. Education has always been an adventure as well as a priority for our family, and I am proud to say we have all been very successful in this area - but that does not mean it was easy. You have comforted me when I was down and calmed me thru the stress, you worried for me when I stayed up late and supported me in every endeavor, you gave me advice, made plans and cheered for me. There have been sleepless nights and early mornings but you have been there through everything and at this great moment of accomplishment I have each of you to thank for getting me to where I am today. You will forever be in my heart and on my mind and I will always remember that you are my anchors in life.

I could not have completed my graduate studies, this research, or my thesis without all of you! I wish you ALL the best of luck in your future endeavors! God speed! GO LOBOS!

Wafer Level Characterization of Infrared Detectors

By

Teressa Rose Specht

B.S. ELECTRICAL ENGINEERING
UNIVERSITY OF NEW MEXICO, 2012

M.S. ELECTRICAL ENGINEERING
UNIVERSITY OF NEW MEXICO, 2016

ABSTRACT

Thermal detector technology such as microbolometers have become more commercially available and affordable in the past five years primarily driven by a manufacturable wafer level fabrication process for these detectors. A recent DARPA program called Wafer level Infrared Detectors (WIRED) is exploring new integration schemes for developing low cost photonic detectors, which have higher speed and sensitivity compared to thermal detectors. Such efforts will require wafer level characterization of photonic detectors with rapid throughput of figures of merit. This thesis compares the performance of mid-wave

infrared (MWIR) photonic detectors using a conventional cryostat and a micro-manipulator probe station to extract specific figures of merit needed to assess the device performance. Two different strained-layer super-lattice mid-wave infrared (3-5.5 μm) detectors were characterized using each system to benchmark their performance in these two systems. The results show that the micro-manipulated probe station test system is quantifiably similar to the cryostat research test system to within a 5% error over a large temperature range (300K - 150K). Below 150K, the dark current in the micro-manipulator probe station test setup was higher than the cryostat test setup. This could be due to the background illumination in the probe station or inadequate thermal contact. By undertaking some diagnostic measurements, it was found that the cause of the discrepancy was the thermal offset between the micro-manipulator probe station sample mount and the leadless chip carrier (LCC) carrying the sample. This thermal offset was due to a mismatch of thermal conductivity and coefficient of thermal expansion (CTE) that led to the delamination of the LCC from the sample mount due to the inadequate thermal contact between the two surfaces. To ensure thermal contact, fastening the LCC to the sample mount would improve the probe station performance to be similar to the cryostat at temperatures below 150K. Because the probe station is designed to characterize detector material without tedious wirebonding and expensive leadless chip carrier waste, we can conclude it can be used to characterize detectors at the wafer level providing a higher throughput compared with a traditional cryostat. This work will allow future detector characterization to be completed using a probe station instead of a traditional cryostat test system, thereby reducing the test and measurement time for infrared detectors.

CONTENTS

LIST OF FIGURES

LIST OF TABLES

1 INTRODUCTION

Over the last 40 years infrared detectors have developed into major contributors to advanced technological applications such as medical imaging, military vision products, industrial manufacturing processes, and other imaging applications. [1] [2] The diverse span of these technological applications displays the advantages of using unique features of infrared detectors that provide more information than what can be measured by other technologies. These applications have propelled material research, such as microbolometer technology, to rapidly develop low cost infrared thermal detectors into a large scale commercial operation seen in industry today.

The bolometer success story shows that thermal detectors are on a direct path to saturating the market with affordable high spatial resolution technology. However, research has also proven that thermal detectors have limitations in speed and sensitivity. In contrast to the thermal detectors' limitations, photon detectors have consistently performed with both higher sensitivities and speed. [3] As the infrared detector market is pushing for more sophisticated detectors for their products, infrared photon detectors are answering the call to perform at this more sophisticated level and are on track to follow the same trend as thermal detectors. Industry is projecting infrared detectors will also become commercially available through the same wafer level integration technology that has made thermal detectors so successful. However, in order for photon detectors to become more commercially available, novel wafer level fabrication and characterization techniques need to be realized. Research and development (R&D) entities have attempted taking on this task; particularly, a DARPA initiative that was implemented in 2015. [4]

This initiative, called WIRED or Wafer Scale Infrared Detectors is set up to fund and moderate R&D projects into providing high performance, low-cost infrared imagers. For example, Figure 1 shows an infrared photon detector fabricated at a wafer level scale.

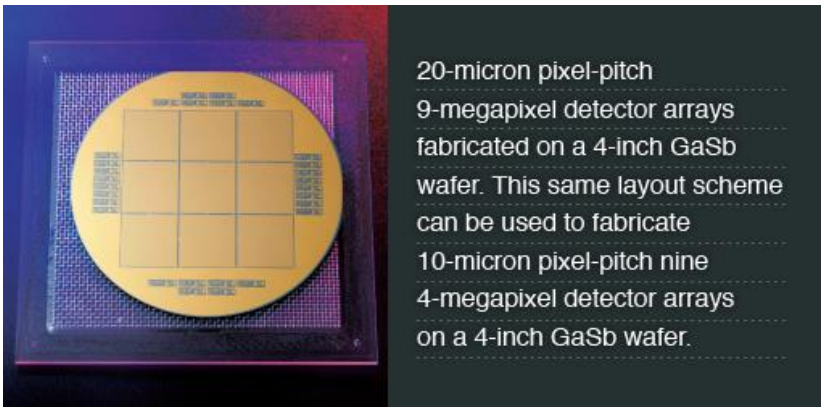

Figure 1: GaSb infrared detector focal plane array wafer grown and fabricated at the Microdevices Laboratory at Jet Propulsion Laboratory. [5]

If radiometrically measuring the entire wafer for quality and uniformity without damaging the material could be successfully completed, there would be more efficient development processes to provide quality assurance on these detector arrays; the result, a faster throughput to lower manufacturing cost, and conclusively, a commercial product that is more affordable.

In order to close the gap between the commercial availability of thermal detectors and photon detectors, research and development entities will need to concentrate on building more robust photon detectors for higher operating temperatures and create a more efficient manufacturing process. The common way to characterize infrared (IR) detector material requires wafer dies to be cleaved and wirebonded to leadless chip carriers (LCCs) as seen in Figure 2 that are then installed in cryostats as a common characterization technique. This process is time consuming and has several limitations, including the number of devices available to characterize at one time. One way to

overcome these limitations is to switch to a probe station characterization technique. Probe stations offer several advantages, such as direct wafer probing and more testing area to characterize more devices at once. However, the question remains if it can be proven to measure detector performance to the same quantifiable accuracy as the common characterization technique. This research aims to kick-start the improvement process for IR photon detectors by offering quick and reliable feedback via probe station characterization without the detector packaging. The main objectives to uncovering some answers to improve the characterization process and the bulk of this research are described in the following:

Contributions of this thesis:

- Compare two different characterization setups: the leadless chip carrier cryostat and the micro-manipulated probe station; pointing out the pros and cons of each setup.
- Qualify the probe station as a setup using Figures of Merit such as dark current, spectral response, responsivity, and quantum efficiency.
- Conclude the probe station is more effective to use as a test setup for wafer level characterization because the advantages outweigh the advantages from the cryostat for wafer level measurements.

This research focuses on the characterization of infrared photodetectors, specifically antimony-based strained-layer super-lattice (SLS) structures that are sensitive to the mid-wave region of the electromagnetic spectrum. We are interested in improving the characterization techniques used to determine detector quality in order to fulfill the growing need of producing commercial high-quality infrared photodetectors. To

demonstrate this characterization process, two different cryogenic research test systems were individually used to measure the same strained-layer super-lattice mid-wave infrared (MWIR) detector. One system is a cryostat test system, while the other is a micro-manipulated probe station test system. The measurements were then compared to benchmark the two cryogenic research test systems to quantitatively define the measurement gap between them.

Results show the micro-manipulated probe station is experimentally comparable to the well-established cryostat test system in the temperature range of about 150K to 300K. Since the micro-manipulated probe station is designed to characterize minimally processed detector material without wirebonding and leadless chip carrier use, we can conclude it can characterize material faster than a traditional cryostat. Through extensive material characterization and testing on single pixel technology produced at the research and development level, the proven techniques and processes learned can be implemented into a commercial manufacturing level.

The first chapter of this thesis has introduced the main motivation for this work and described the questions this research is trying to answer through experimental study of these two research test setups. The second chapter will describe the basics of infrared detector theory and operation, as well as the specific detector characteristic differences between photon detectors and thermal detectors. This chapter will also discuss the reference photon detectors chosen to complete the characterization, the general methods of photodetector characterization, and the different test setups used to measure the detector's characteristics. These characteristics, or Figures of Merit, will be described in further detail in the third chapter as well as how they are measured with each test setup to

wrap up all introductory material required to understand the experimental results. Finally, the results of the experiment will be presented, and a discussion of the results and future work will conclude the thesis in the fourth and final chapter.

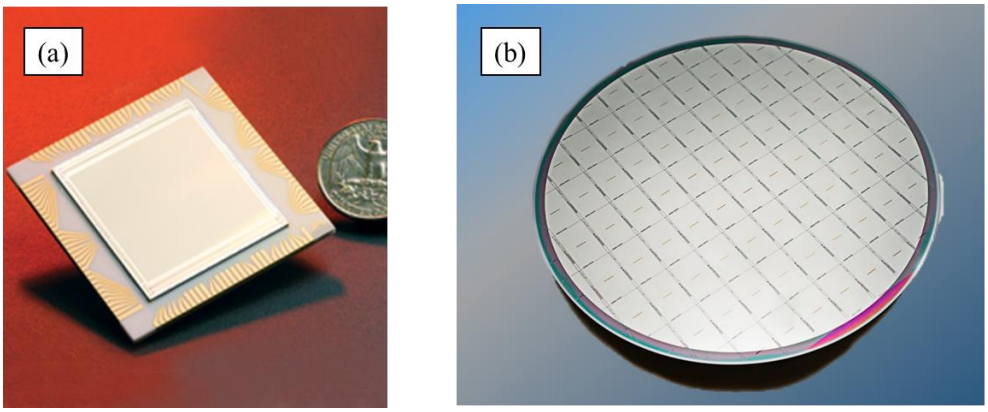

Figure 2: Manufactured and Fabricated Infrared Detectors. (a) Single Quantum Well Infrared Photodetector Focal Plane Array on an LCC. (b) Multiple Thermal Detectors on Wafer. [6] [7]

2 MATERIALS & METHODS

This chapter introduces the fundamentals of infrared detector operation in order to understand the physics of the detection process. Once some basic concepts are presented, a discussion on thermal detectors and photon detectors will give some perspective on the pros and cons of each type of detector. The single pixel detectors used as reference detectors for this work will be described along with their material structure and comments about their individual characteristics. Finally, the methods used to characterize these photon detectors and the research test setups will be discussed to give some background on the experimental equipment used in this study.

2.1 INFRARED DETECTOR BASICS

Infrared detector technology has enabled the development of scientific devices that expand the knowledge of invisible energy through measurement of the electromagnetic spectrum. These detectors are sensitive to specific wavelengths of light around the infrared region in the electromagnetic spectrum as shown in Figure 3. This figure identifies all possible wavelengths of electromagnetic radiation and classifies all regions within the spectrum. Each region is identified by wavelength, frequency, and energy; visible light is only a fraction of the spectrum.

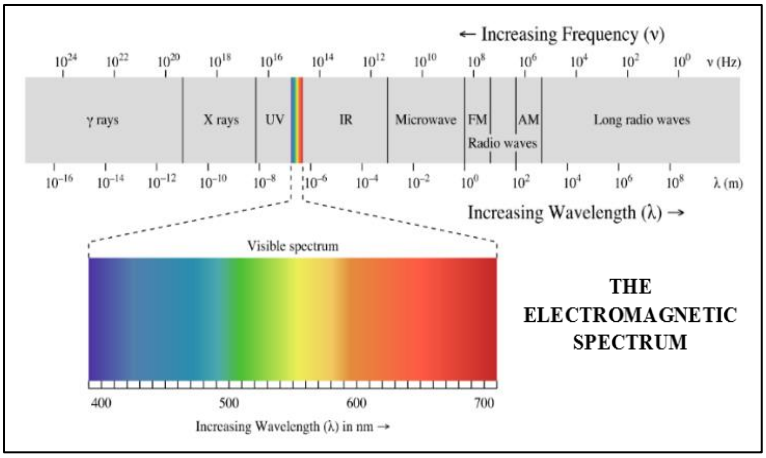

Figure 3: The Electromagnetic Spectrum Diagram of the Different Regions along the Entire Spectrum with an Emphasis on the Visible Spectrum [8]

Based on the natural divisions of each region using the wavelength, frequency, and energy level, different technological applications can be classified using the response between the radiated, transmitted, and absorbed electromagnetic energy. [9] [10] For example, radio waves are defined as any frequency between about 1kHz and 1THz, and are used for long-distance communication, particularly with satellites. [11] This frequency range is defined using the historical theories established by Hershel and Maxwell during the 1800's. [11] As Hershel, Maxwell, and other scientists shaped each region, they deemed the infrared region to be within the wavelength range of 750nm – 1mm with a frequency range of 400THz – 300GHz respectively.

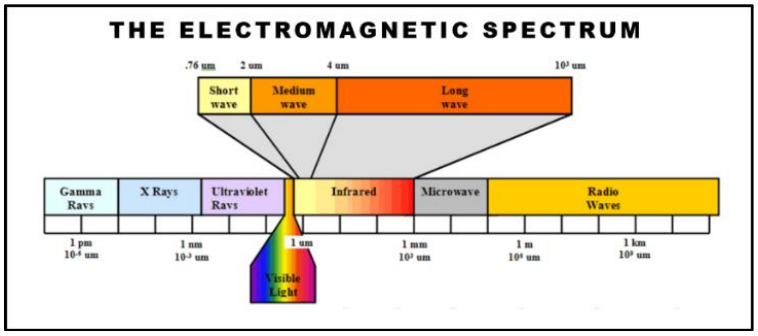

Figure 4: Different Regions in the Infrared Section of the Electromagnetic Spectrum - Short-Wave, Mid-Wave, and Long-Wave [8] [12]

Like the natural divisions within the entire electromagnetic spectrum, there are segments that break each region into further sections. In the infrared region of the electromagnetic spectrum, there are regions that are defined by natural phenomenon in the atmosphere where the light transmission of the atmosphere can either pass through or be blocked by absorbing molecules such as H_2O, CO_2, and O_3 as seen in Figure 5. These regions are called spectral bands. There are four spectral bands that can describe the wavelength region where detector's sensitivity lies: near infrared (0.75μm – 1.4μm); short-wave infrared (1.4μm – 2.5μm); mid-wave infrared (3μm – 5μm); and long-wave infrared (8μm – 15μm) which also includes very long-wave infrared (15μm – 1mm). Each region has specific applications associated with them because of the individual detector's material properties.

For example, the near infrared can be used for night vision technology – such as night vision goggles – by collecting small amounts of ambient light through an optical lens to push through a Gallium Arsenide photocathode that converts the light to electrons for amplification and is "read" by a phosphorous screen to show the user the image created by the resulting photons. [13] The short-wave infrared is most commonly used for optical communications – recognized for telephone communication lines – where the standardized 1550nm wavelength laser light is ideal to use with the silica-based fiber due to the combination of low attenuation and total internal reflection at 1550nm. [14] Along with additional electronics to interpret the light at either end, the ultimate results consist of data network communication such as the Internet. [15] Applications of the mid-wave infrared vary widely, but one particular example is global surveillance satellites with large staring focal plane array (FPA) cameras. The materials used to create MWIR FPAs

have many good qualities to provide high performance under the harsh space environment, such as great atmospheric transmission and radiance parameters. [16] Like the mid-wave region, the long-wave infrared also has many applications – such as facility diagnostics – by using the temperature differences based off of the amount of radiation emitted by an object as temperature increases. [9] While this discussion proves there are many different infrared detectors, only those of the same class should be compared to one another because of their different characteristics, physical mechanisms, and operating wavelength ranges. For instance, only MWIR detectors should be compared with other MWIR detector and only LWIR detectors should be compared with other LWIR detectors. This research was conducted using only mid-wave infrared detectors.

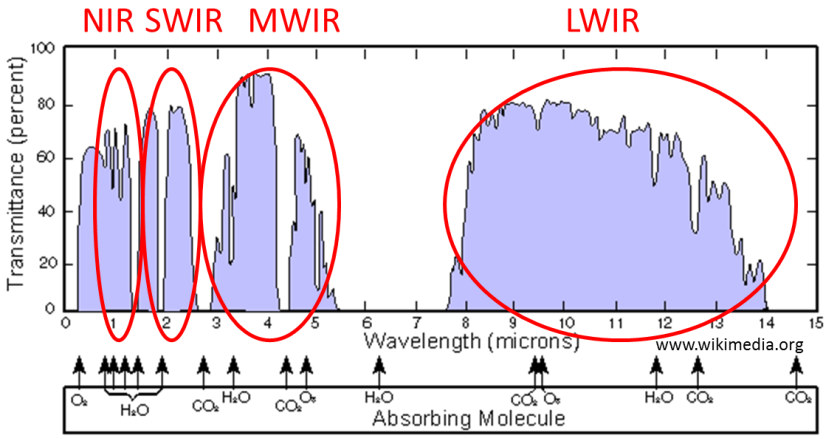

Figure 5: Plot of atmospheric transmittance in the infrared region [17]

For mid-wave infrared detectors, there are two types of detectors that are widely used: thermal and photon. When heat is absorbed into a thermal detector material, a change in the detector's material properties occur. Thermal detectors sense and measure that property change electrically. An example of this is a pyroelectric detector; these detectors use the pyroelectric effect to detect infrared radiation from an object using internal material polarization to see small changes in temperature. [18] Photon detectors

measure the direct conversion of photons to electron-hole pairs through the bandgap of semiconductor materials. An example of a photon detector is an Indium Antimonide (InSb) photodetector; this semiconductor material uses the photovoltaic effect to generate electric current when exposed to infrared radiation, also known as photons, with energy levels in the infrared region. [9] Several notable characteristics of thermal detectors and photon detectors can be found in Table 1.

Table 1. Comparison of Mid-Wave Infrared Detector Characteristics: Thermal Detectors and Photon Detectors

Mid-wave Infrared Detector Characteristics	
MWIR Thermal Detectors	**MWIR Photon Detectors**
• Heat absorbed into material and change in material properties is detected • Metallic or Semiconductor materials • High Operating Temperature (~295K) • Commercial-off-the-Shelf (COTS) availability • Low cost • Low Sensitivity • Low Speed	• Direct conversion of photons to electron-hole pairs • Semiconductor materials • Low Operating Temperature (~77K) • Limited commercial availability • Expensive • High Sensitivity • High Speed

Pros and cons are highlighted in Table 1 by red (con) and green (pro) to show the differences between thermal detectors and photon detectors. As you can see, the pros and cons are spread evenly across both types of detectors. However, the negative attributes of thermal detectors are low sensitivity and low speed; these are caused by the fundamental operation of thermal detectors, with heat transfer being the detection mechanism. For example, the pyroelectric detector mentioned above can only operate at a maximum signal rate of 13Hz due to the natural response between the material and heat. [19] As a result, thermal detectors are not able to overcome these qualities because heat is sluggish compared to electrons. While photon detectors have been pointed out to have several

disadvantages, their high sensitivity and high speed qualities are enough incentive to develop the low operating temperature and little commercial availability into pros through research and development projects, such as wafer level characterization research.

2.2 Photodetector Characteristics

As the explanation of the general operation of infrared detectors continues, we move into the describing the detectors used to complete this study. To reiterate, photodetectors are detectors that directly convert photons to electrons by using the bandgap structure within the material. The detectors below are strained-layer super-lattice infrared detectors with complex bandgap structures; but despite the detector structure, they still use the fundamental theory of direct atomic interaction of light onto the lattice of the material to produce an electrical signal. [9]

2.3 Reference Detector Descriptions

For the sake of simplicity, the two infrared detector samples that were used in this experiment have been labeled as Sample A and Sample B. Both strained-layer super-lattice mid-wave infrared (MWIR) detectors have been grown at the Center of High Technology Materials (CHTM) as research-based structures for the Krishna detector group. While they were grown and fabricated at CHTM, their characteristics are different; therefore, brief descriptions of the physical characteristics of each sample are described.

2.3.1 Sample A: MWIR Strained-Layer Super-Lattice pBn Detector

Sample A is a strained-layer super-lattice mid-wave infrared pBn detector structure with a variable area detector array mask to create detectors for single pixel measurement as shown in Figure 6.

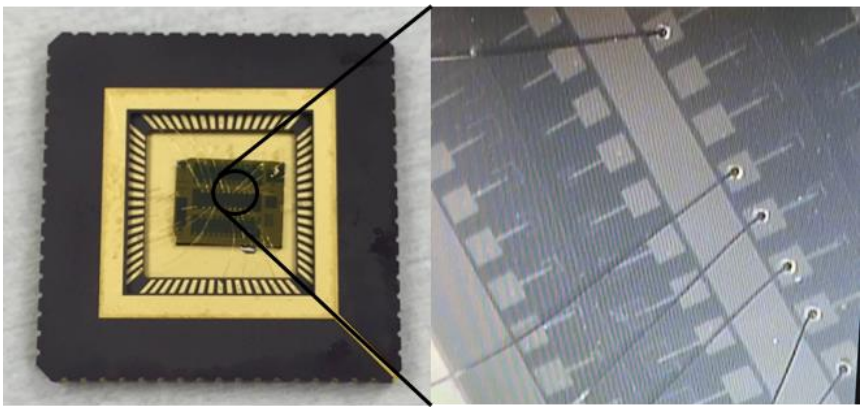

Figure 6: SAMPLE A - Mid-Wave Infrared Strained-Layer Super-lattice pBn Detector mounted on a 68 pin LCC and wirebonded out to LCC pads

The pBn detector was grown at CHTM using the Veeco Gen10 Molecular Beam Epitaxy (MBE) and was fabricated in the CHTM clean room facilities. The individual layer descriptions are shown in Figure 7 below.

G16-003 pBn
DETECTOR STRUCTURE

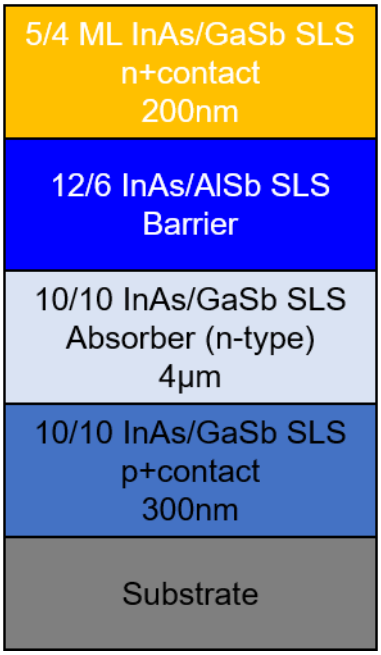

SAMPLE A
LAYER DESCRIPTIONS

n+contact Layer

- Top contact for structure

Barrier Layer

- Blocks carriers from recombining

Absorber Layer

- Lattice mismatch between p+ and Barrier corrected with this layer
- Light absorption layer where holes are free to move from the absorber to the contact

p+contact Layer

- Hole transport through contact

Figure 7: Graphical Representation of Sample A G16-003 pBn Detector Layer Structure and Layer Descriptions

The mask pattern was designed to be a variable area detector array to test multiple single pixel area sizes of the same detector material. Several device sizes were used throughout the testing phase to get an idea of the material's uniformity. The device sizes used on the sample for this experiment were chosen based off of detector area: 100µm, 175µm, 250µm, and 500µm. Since the mask pattern has a square aperture design for each device, each detector area can be calculated as the length squared. One final note, the detector cutoff wavelength is 5.1µm based off of the spectral response measurement plotted in Figure 8. A long-pass filter that was used in the responsivity measurement is also depicted in Figure 8 to show the spectral response of the filter relative to the spectral response of the detector; the filter data will be elaborated further in Chapter 4.

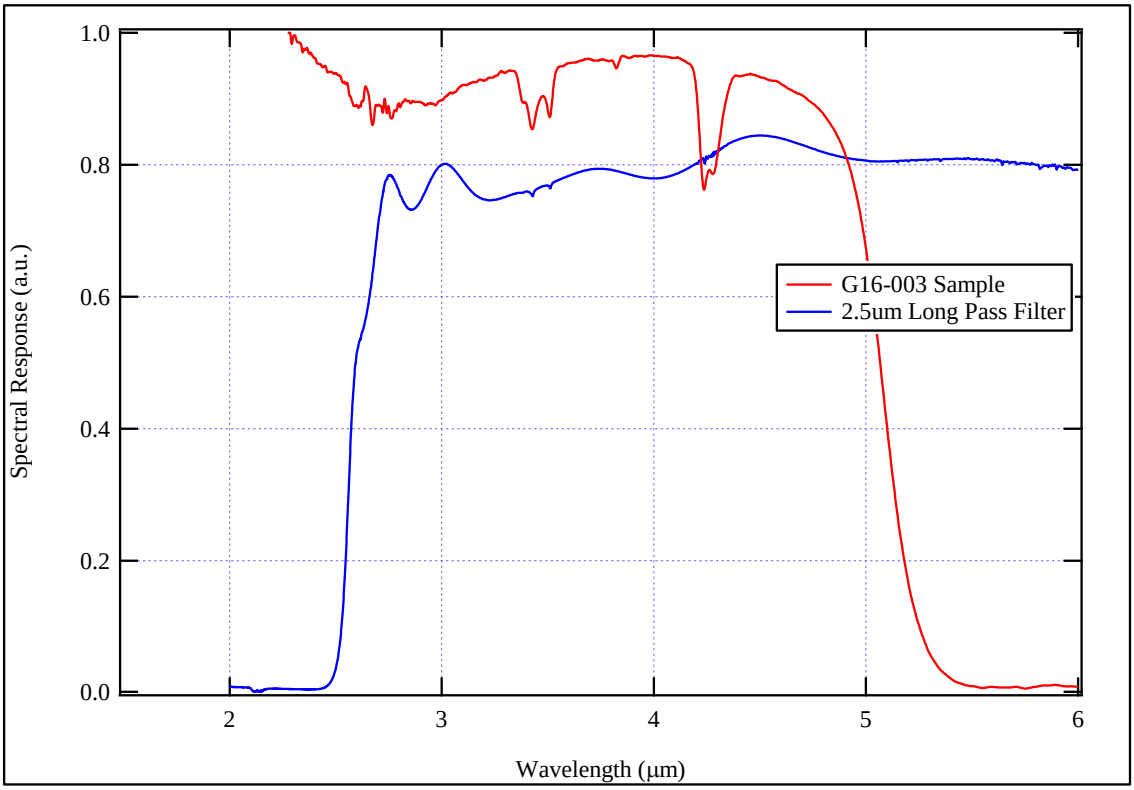

Figure 8: G16-003 MWIR SLS pBn Detector Spectral Response with 2.5um Long-Pass Filter

2.3.2 Sample B: MWIR Strained-Layer Super-Lattice pin Detector

Sample B is a strained-layer super-lattice (SLS) MWIR pin detector structure with a variable area detector array mask to create detectors for single pixel measurement as shown in Figure 9.

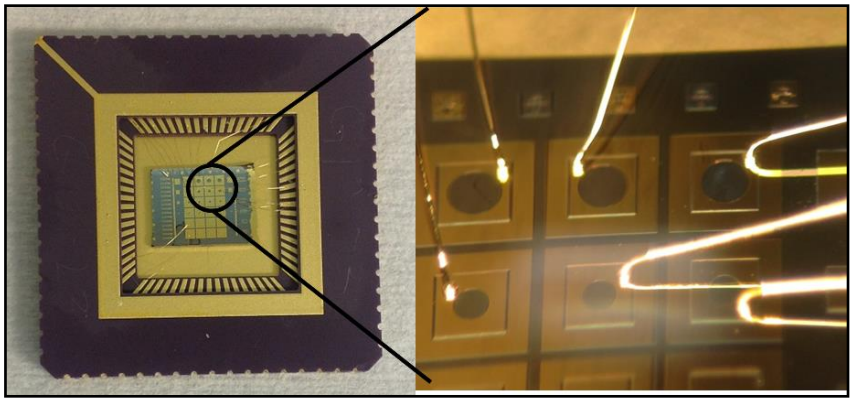

Figure 9: SAMPLE B - Mid-Wave Infrared Strained-Layer Super-lattice pin Detector mounted on a 68 pin LCC and wirebonded out to LCC pads [20]

The pin detector was grown at CHTM using the CHTM Left-Hand-Side Molecular Beam Epitaxy (MBE) and was fabricated in the CHTM clean room facilities. The individual layer descriptions are shown in Figure 10 below.

L12-56 pin
DETECTOR STRUCTURE

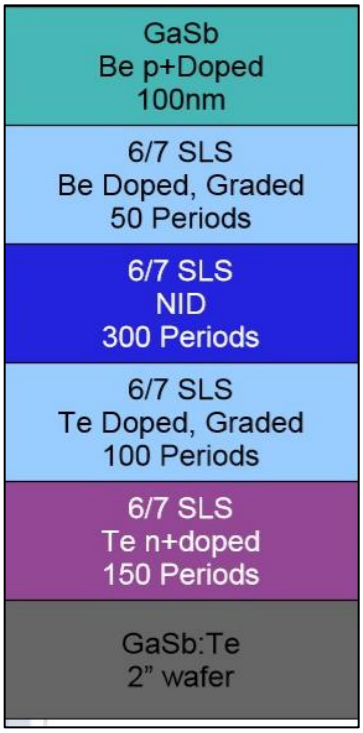

SAMPLE B
LAYER DESCRIPTIONS

p+Doped GaSb Layer

- Top contact for structure

Graded SLS Layer

- Graded doping to improve carrier transport to the contacts

NID Layer

- Absorber layer

Graded SLS Layer

- Graded doping to improve carrier transport to the contacts

n+doped SLS Layer

- Bottom contact

Figure 10: Graphical Representation of Sample B L12-56 pin Detector Layer Structure and Layer Descriptions

The mask pattern was designed to be a variable area detector array to test multiple area sizes of the same detector material. Several device sizes were used throughout the testing phase to get an idea of the material's uniformity. The device sizes used on the sample for this experiment were chosen based off of detector diameter length: 150µm, 200µm, and 300µm. Since the mask pattern has a round aperture design for each device, each detector area can be calculated as the area of a circle. One final note, the detector cutoff wavelength is 3.2µm based off of the spectral response measurement of the detector in Figure 11.

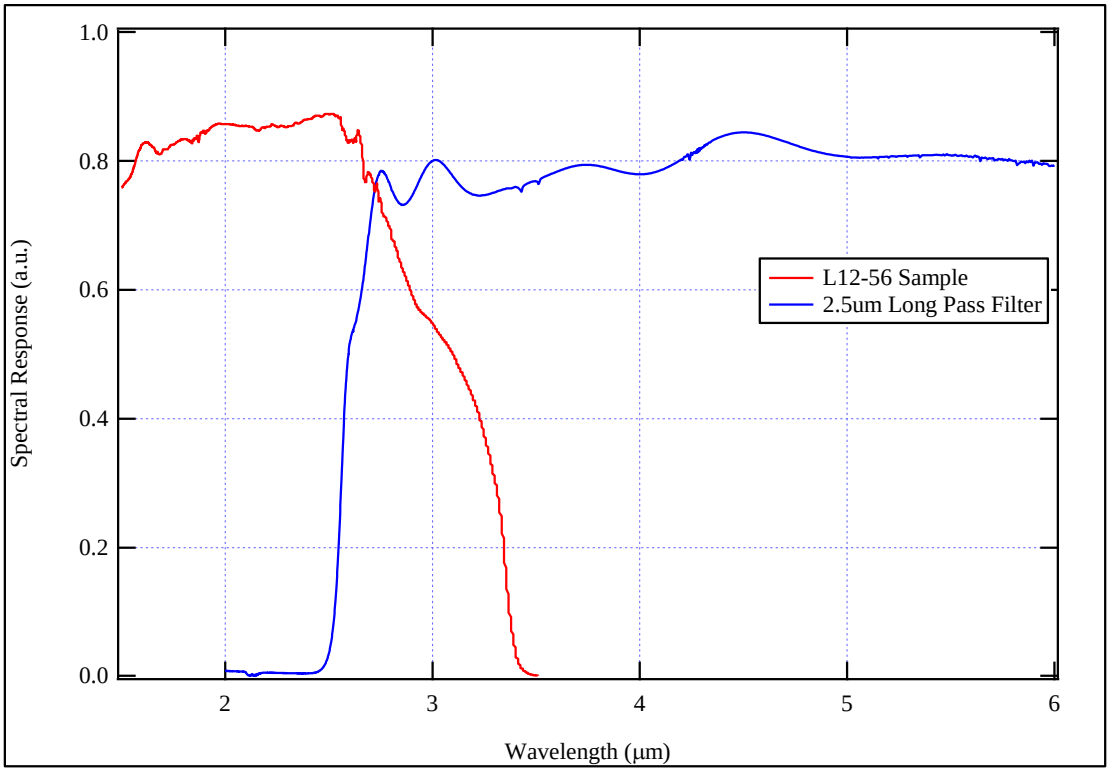

Figure 11: L12-56 MWIR SLS pin Detector Spectral Response with 2.5um Long-Pass Filter

2.4 CHARACTERIZATION

Discussing the photodetector operation in detail brings about the question of the quality of the detector. Determining the quality of the detector includes testing it under various operating conditions it would typically undergo during its lifetime. Characterization, or determining the performance characteristics of the detector, consists of testing the detector using measurement tools to acquire parameters called Figures of Merit. Figures of Merit will be discussed later in Chapter 3, but generally they define the detector operation experimentally. Characterization is an important part of the infrared detector industry because it allows the community to quantify and compare sensor

performance to theoretical specifications or other device designs whose performance has been reported. For example, only thermal detectors should be compared with other thermal detectors because they have similar performance measures and belong to the same infrared detector family thus driving the different characterization techniques used for these detector regions. The following parameters are defined for use in this chapter:

c = speed of light ($3x10^{8}$ m/s)

k_B = Boltzmann's constant ($1.38x10^{-23}$ J/K)

h = Planck's constant ($6.6x10^{-34}$ J/s)

P = power transferred

ε = emissivity of the source (ideal = 1)

ΔA_s = incremental source area

θ_s = angle between the line connecting the two surfaces and a perpendicular to the source surface

ε = absorptivity of the collector or detector (ideal = 1)

ΔA_r = incremental receiver area (detector area)

θ_s = angle between the line connecting the two surfaces and a perpendicular to the collector surface

$M(\lambda, T)$ = spectral exitance

$\Delta\lambda$ = spectral bandwidth of interest

r = distance between the source and the detector

τ = transmittance of all optics in optical path

Ω = solid angle

E_q = irradiance

L_e (λ, T) = source radiance

θ = field of view (FOV) angle

F/# = F number

2.4.1 Radiometry and Radiometric Measurements

Radiometry is defined as the optical techniques used to determine the amount of radiation on the detector given the geometry of the optical system and the source's radiative power. As a result, radiometry gives the ability to predict the electromagnetic power transfer between the source and detector. [10] The general equation to determine the prediction of power transfer is given as the Incremental Power Transfer equation:

$$P = \left(\frac{(\varepsilon A_s \cos\theta_s)(\alpha A_r \cos\theta_r)}{\pi r^2}\right)\tau M(\lambda, T)$$

There are several geometric configurations in which a radiometric setup can be identified. The configurations most commonly used are: Extended Source, Point Source, and Finite Source. [9] All of these configurations depend on the geometry between the source and the detector. For this experiment, the radiometric configuration used to determine the source's radiative power onto the detector is an extended source configuration as depicted in Figure 12. An extended source configuration is identified to have a Lambertian source, fully illuminating the detector where the limiting aperture is on the detector side of the radiometric setup.

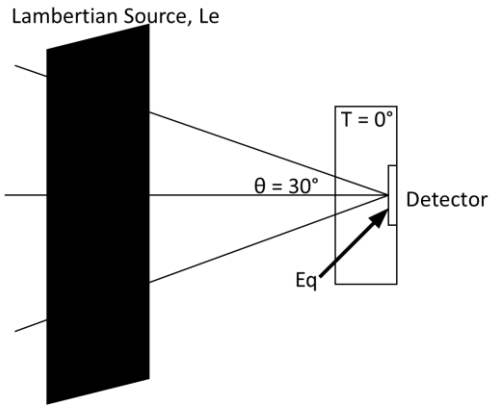

Figure 12: Extended Source Radiometric Setup and Geometry Used for Extended Source Configurations [9]

The equations used to describe the extended source measurements are as follows:

$$\Omega = \frac{A_r}{r^2}$$

$$E_q = \pi L_e \sin^2\theta = \frac{\pi L_e}{4\left(\frac{F}{\#}\right)^2 + 1}$$

Radiometric measurements need to be very precise for a low error between the calculated value and the measured value. For example, if the distance measured between the detector and the source is not precisely or correctly measured, there will be an error between the calculated value and the measured value of the irradiance by a squared factor due to the solid angle calculation. A percent error that is squared can result in a large overall error, falsifying the quantitative characterization of the photodetector. One key element to radiometric measurements is the blackbody; a blackbody is a unique source that emits radiation at unity emissivity. A blackbody radiation curve is defined by Planck's Law shown in the following equation and in Figure 13.

$$L_e(\lambda, T) = \frac{2hc^2}{\lambda^5\left(e^{hc/\lambda k_B T} - 1\right)}$$

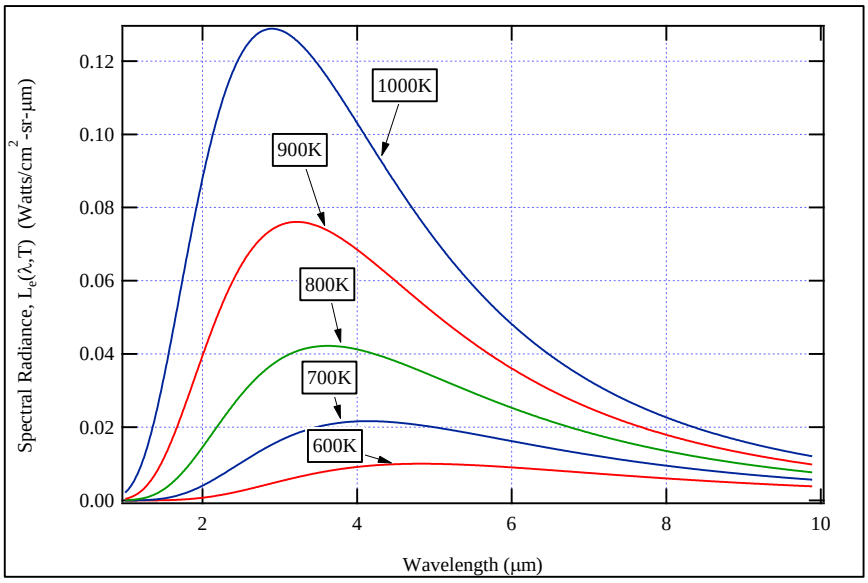

Figure 13: Planck's Law for Radiant Spectral Exitance vs Wavelength

The culmination of figure of merit measurements will give the quantitative comparison between the two different cryogenic research test setups being pursued by this research.

Special equipment and tools are required to complete photodetector characterization measurements. Most laboratory spaces have this equipment available because they are used in many measurement applications. For instance, a lock-in amplifier is used to measure the photodetector output. For this experiment, the characterization setups in Figure 14 were used to measure the photodetector dark current, spectral response, and responsivity. These characterization setups are generally used for all photodetector characterizations, but in some cases the photodetector specifications could dictate the test methods to be different. More discussion on the characterization setups can be found in Chapter 3.

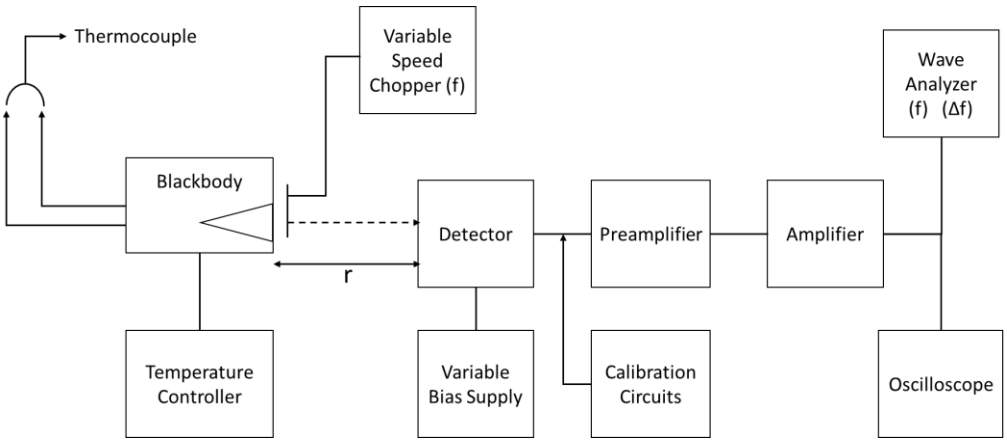

Figure 14: Schematic of Typical Lab Setup to Measure Detector Performance through Figures of Merit [10]

2.5 Research Test Setups

Characterizing the photodetectors appropriately required specific equipment to measure each device, known as cryogenic research test systems. This test equipment is well-established and is used extensively in a variety of research and development environments when characterizing photodetectors. [10] While the cryogenic research test setups vary, the mechanics can be simplified to the structure of a Dewar. Dewars were first created by Sir James Dewar, who found that a vacuum-insulated flask could prevent cryogens (such as liquid nitrogen) from boiling off rapidly. [10] The components of a generic pour filled Dewar are seen in Figure 15, which shows how the vacuum chamber is used to protect the cryogens from the outside atmosphere and how the reservoir used to hold the liquid cryogens. To clarify, liquid cryogens are commonly known as purified gases in their liquid state at low temperatures. [21] A list of gases commonly used as liquid cryogens are listed in Table 2.

Table 2. Normal Boiling Point (NBP) Temperature of Cryogenic Gases at One Atmosphere Pressure [21]

Cryogen	(K)	(°C)	(°R)	(°F)
Methane	111.7	-161.5	201.1	-258.6
Oxygen	90.2	-183.0	162.4	-297.3
Nitrogen	77.4	-195.8	139.3	-320.4
Hydrogen	20.3	-252.9	36.5	-423.2
Helium	4.2	-269.0	7.6	-452.1
Absolute zero	0	-273.15	0	-459.67

Typically liquid nitrogen (77K – 295K) and liquid helium (4K – 295K) are used to cool down photodetectors for testing. Liquid oxygen (90K – 295K) may be used from time to time to achieve specific temperatures, however, is its rather expensive to procure ultimately making liquid nitrogen (LN2) the primary choice for the temperature range between 90K – 295K.

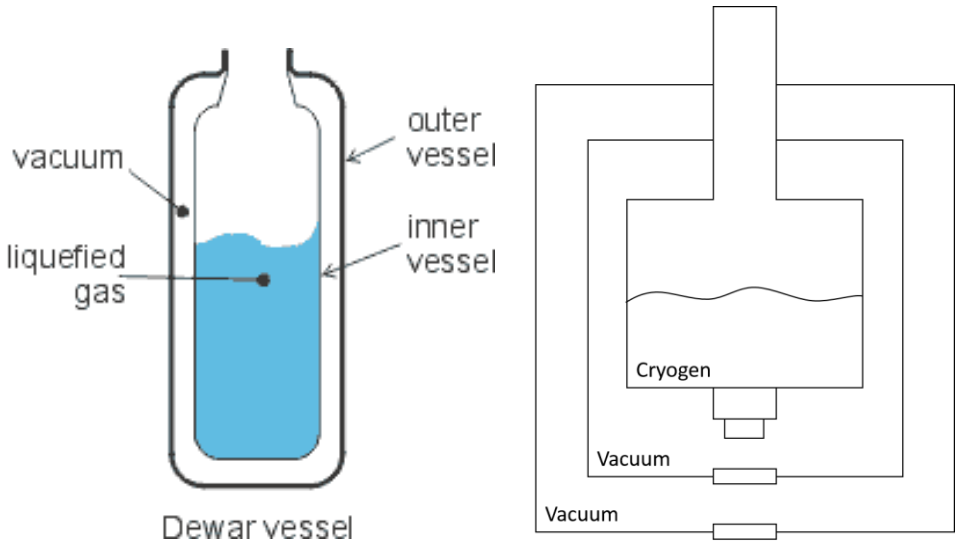

Figure 15: Generic Dewar Vessel [22] (left) which shows the basic application of holding cryogens in their liquid states; Typical Cryostat Structure (right) shows the basic structure required to set proper environmental properties for a device under test at low temperatures

The Dewar configuration becomes more complex to accommodate a suitable testing environment for the devices under test, such as simulating space-like conditions where there is little to no atmosphere and temperatures are frigid due to the lack of atmosphere. Because the device under test can't be in direct contact with the liquid cryogens for radiometric measurements, the Dewar's vessel is expanded by designing an open space to fit the device and its electronics which is typically known as the test chamber; this is the point in which the dewar becomes the cryogenic research test system. As seen in Figure 15 a schematic of a typical cryogenic research test system show a device under test and optical capabilities to complete radiometric measurements on the device.

Some of the features in the figure can be further described to clarify their function within the test system.

Cryostat Shields:

The shields in the test system perform two functions – they 1) provide a chamber to thermally isolate the device under test from the outside radiation, and 2) they provide a clean, dry atmosphere using the vacuum process. The outer vessel is created by the outmost shield or the 300K shield. It is usually populated with interconnect ports that are sealed with o-rings and potted connectors to provide a way for the user to interact with the test system electrically or mechanically. The chamber is evacuated with a turbo pump designed to extract any particles out of the chamber. This evacuation should go down to a preferable pressure of $1x10^{-5}$ atmosphere(atm, or0.0076 torr) in order to create the ultra-high vacuum needed to test the detector safely. If the cryogenic research test system does not meet this pressure, moisture and other particles can be present in the test system, possibly contaminating the sample under test and degrading the test conditions.

Mounting surface:

The devices under test are installed and strapped to a highly thermally conductive metal pedestal or a “cold finger” that is in direct thermal contact with the liquid cryogen reservoir. Usually a temperature sensor is fastened to the pedestal to notify the user of the operating temperature of the device during testing. A resistive heater is also installed to bring the pedestal up to the desired device operating temperature for the measurement.

Optical window:

In order to radiometrically characterize the devices, a port is needed to allow use of a controlled light source, such as a blackbody radiation source. The optical window or windows can provide optical axis capability to the system. The optical axis is defined as the direct invisible line strung out as the shortest distance between the device under test and the radiation source. As described earlier, the radiometry measurements will use the optical windows as components in the optical system to determine the distance, spot size, and transmission impacting the radiance projected onto the device under test. Various transmission windows are installed in these ports that block out any unwanted light and are selected based off of the transmission properties of the window material. This allows the user to customize the radiometry and optimize the test setup using a band pass approach of controlling the light entering the optical system.

Cryogen reservoir:

The vessel that holds the cryogens, which is thermally strapped to the pedestal, is the cooling mechanism for bringing these photodetectors down to low measurement temperatures. Since these photodetectors do not perform well at warmer temperatures, the reservoir needs to be able to provide enough cold to keep the detector at a uniform

temperature throughout the measurement. There are different avenues used to cool a test system, such as: closed-cycle coolers, continuous flow cryostats, and pour filled open reservoirs.

2.5.1 Cryostat Test System

Figure 16: Example of a Standard Cryostat Research Test Setup from Janis Research Co. [23]

The first cryogenic research test system presented and used to characterize the detectors for this project is a well-established piece of equipment called a cryostat. A cryostat is a mechanical system built much like the typical cryogenic research test system as described above. This particular cryostat consists of four window ports in the outer shield, four smaller ports in the inner shield and a pedestal with a 68 pin leadless chip carrier (LCC) held in-line with the cryostat's optical axis. The KYOCERA leadless chip carrier was purchased from Spectrum Semiconductor Materials, Inc. [24] [25]

2.5.2 Micro-manipulated Probe Station Test System

Figure 17: Example of a Micro-manipulated Probe Station Research Test Setup from Janis Research Co. [26]

The second cryogenic research test system is a more modern take on the cryostat as it is similar in function, yet the sample doesn't have to be epoxied and wirebonded to a leadless chip carrier in order for it to be characterized.

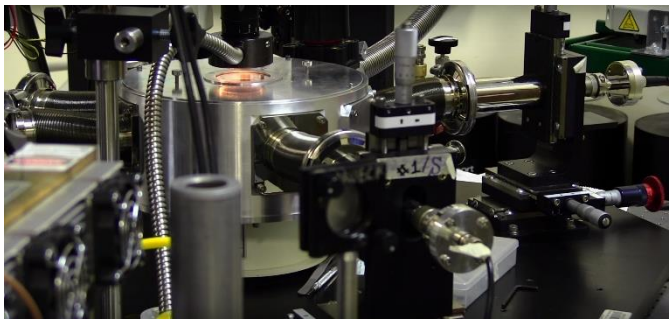

Figure 18: Close-up View of the ST-500 Micro-manipulated Probe Station Used as the Probe Station Research Test Setup Being Compared with the Cryostat Research Test System

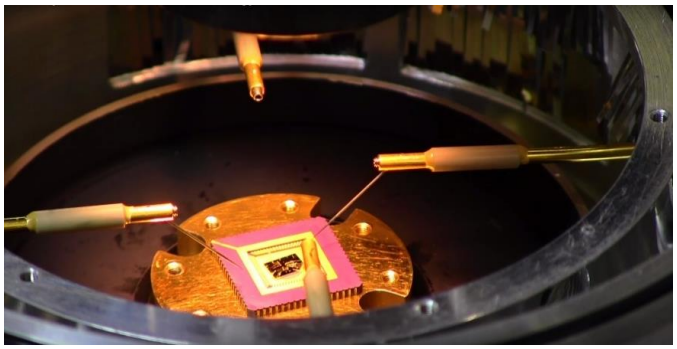

Figure 19: A Detector Sample Sits on the Sample Mount of the ST-500 Micro-manipulated Probe Station with Thermally Strapped Probes Off of the Sample and Out of Measurement Position

2.6 SUMMARY

In this chapter, the infrared detector basics were introduced in detail. The wavelength correlation between the detector and the rest of the electromagnetic spectrum was presented by giving an overall explanation of the electromagnetic spectrum and the material characteristics of the reference strained-layer super-lattice mid-wave infrared (MWIR) detector samples used for this research. Characterization principles and measurement techniques were discussed along with general radiometry theory that covers the incremental power transfer equation, illustrating the energy transfer between the source and detector in a typical extended source radiometric system. Finally, the two test setups used for this work were presented in detail.

3 FIGURES OF MERIT

Now that the physics and mechanics of typical photodetectors have been explained, we can continue to show how these photodetectors perform. In this chapter, the measurable parameters used to determine the quality of a photodetector are discussed in detail. These parameters are known as Figures of Merit, which enable the electro-optical community to compare the relative performance of different detectors on a standard unit basis. [9] The following parameters are defined for use in this chapter:

q = charge of an electron (1.6×10^{-19} C)

c = speed of light (3×10^{8} m/s)

k_B = Boltzmann's constant (1.38×10^{-23} J/K)

h = Planck's constant (6.6×10^{-34} J/s)

τ = time constant

η = quantum efficiency

f = chopping frequency

$R(\lambda)$ = wavelength dependent responsivity (A/W)

I_{photo} = amplitude of the signal measured by the network analyzer (A)

A_{det} = detector area (cm^2)

A_{bb} = blackbody area (cm^2)

r = distance between the detector and blackbody source (cm)

λ, λ_{cutoff} = wavelength (µm) or detector cutoff wavelength (µm)

$M_{e,\lambda}$ = blackbody spectral radiance as a function of wavelength and temperature

$RR(\lambda)$ = relative spectral response (also known as normalized spectral response)

E_q = incident photon flux density (irradiance) (photons/s-cm^2)

G = 1; photodetector gain is equal to unity for simplicity

D_n,D_p = minority carrier electron/hole diffusion coefficient (cm^2/s)

n_p,p_n = minority carrier electron/hole concentration (cm^{-3})

L_n,L_p = minority carrier electron/hole diffusion length (cm)

3.1 Dark Current

The dark current of a photodetector is one of the most basic measurements to demonstrate initial performance and overall quality. Dark current is described as the current measured across the detector when no incident light or radiation is exciting the detector material. This is also called reverse saturation current in some literature because the dark current is usually observed when the detector is being operated with a reverse bias voltage applied. [9] The lack of incident light on the detector minimizes the optical performance of the detector material, exposing the noise influences on the overall signal due to the random generation and recombination occurring in the depletion region of the detector. [27] This limiting factor of performance can also be influenced by the radiation caused by the surrounding environment's temperature, as well as material defects in the detector. [27] The expressions for dark current are described below:

$$i = i_0(e^{\frac{qV}{kT}} - 1)$$

$$i_0 = q\left(\frac{n_p D_e}{L_e} + \frac{p_n D_h}{L_h}\right) A_d$$

The method for attaining the detector dark current is to measure the current versus bias voltage. As seen in Figure 20, the current-voltage (I-V) curve shows where the dark

current is measured under reverse bias voltage and forward bias conditions. This is done by grounding the bottom contact of the detector and applying the voltage bias across the detector with the top contact. The dark current can be described as the current between the 0V and the measured curve in the reverse bias section of the graph.

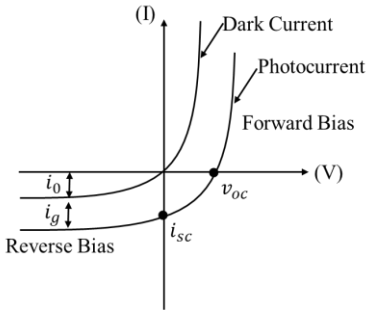

Figure 20: Photodiode current-voltage (I-V) curve with and without incident radiation [9]

The I-V curve can be collected using both the cryostat research test setup and the micro-manipulated probe station test setup as shown in Figure 21 and Figure 22. The cryostat research test setup uses the cryostat (cooled with the closed-cycle LHe compressor), a temperature controller to control the sample or detector temperature of 77K, and a parameter analyzer to source the bias voltage to the two sides of the detector and read the current across the detector simultaneously.

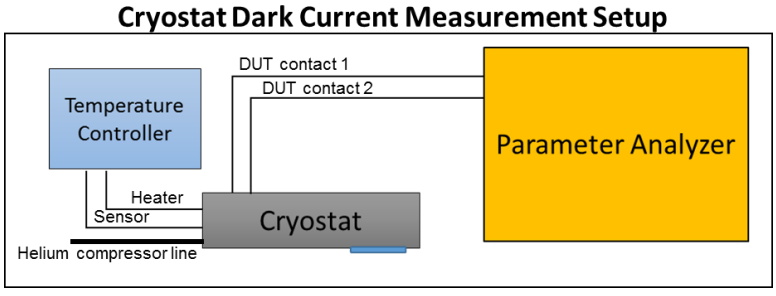

Figure 21: Dark Current Measurement Setup for Cryostat Test Setup

The micro-manipulated probe station test setup measures the dark current using the probe station as a continuous flow of LN_2 cools the sample down to 77K, a temperature

controller to control the sample temperature, and a source measure unit to source the bias voltage to the detector while measuring the current across the detector.

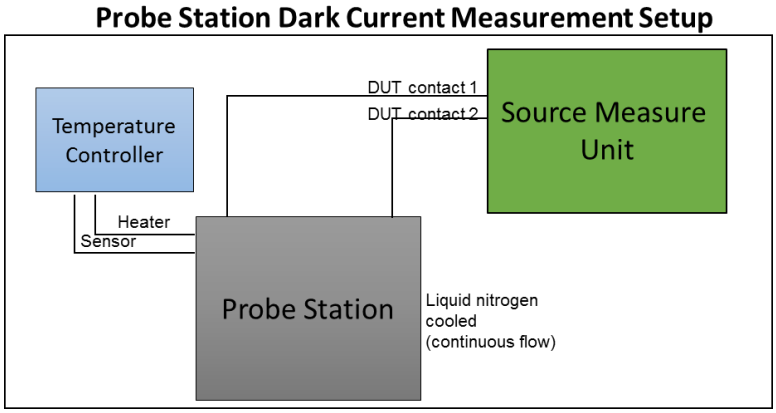

Figure 22: Dark Current Measurement Setup for Micro-manipulated Probe Station Test Setup

3.2 Spectral Response

The spectral response of a detector is a spectrum of the material's molecular absorption and transmission over a wavelength range. [28] This spectral curve information is used for responsivity measurements by using the curve to normalize the responsivity of the detector material. It is also known as relative spectral response RR(λ) or normalized spectral response. To complete this measurement, the material is cooled and the sample detector is connected to a trans-impedance Amplifier (TIA) to amplify the signal. The detector is then biased using the Fourier Transform Infrared (FTIR) spectrometer interface box to take the spectral response at various bias voltages if desired. The sample is subjected to infrared radiation directed by a mirror from the FTIR spectrometer, and the resulting response curve is reported in % transmission in a computer program used to control the FTIR. [29]

The cryostat spectral response setup is identified in Figure 23. The cryostat was the only test setup used for this measurement because it was not possible to measure this parameter with the probe station due to the top-view optical window port on the probe station. The detector samples were cooled to 77K for this measurement and were operated at a 0V voltage bias.

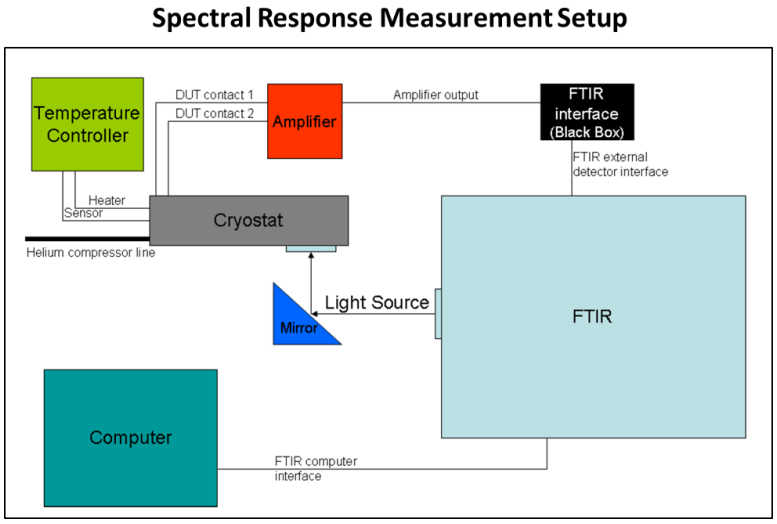

Figure 23: Spectral Response Measurement Setup for Cryostat Test Setup [20]

3.3 RESPONSIVITY

The responsivity of a photodetector is another basic measurement to determine the material's initial quality and performance. This parameter defines how the incident light coming into the detector's field of view is absorbed and converted to an electrical signal at the output of the detector. [9] The input versus output correlation is usually described as a current measurement in amperes per watt, to signify the amount of power output converted from radiant optical power input. It can also be described in other units such as photons per second per centimeters squared. Here are the general equations used for current responsivity:

$$R_i(\lambda, f) = \frac{\eta \lambda q}{hc\sqrt{1 + (2\pi f \tau)^2}} G$$

$$R_\lambda = \frac{\text{Iphoto}}{(A_{bb})\left(\frac{A_{det}}{r^2}\right)\left(\int_0^{\lambda_c} M_{e,\lambda}(\lambda,T) RR(\lambda) d\lambda\right)} \left(A/W\right)$$

The output responsivity of a detector is calculated given the incident photon flux of the calibrated blackbody being used, which depends on the blackbody temperature. The radiometric characterization setup that was pointed out earlier in Chapter 2 is considered during responsivity measurements due to the power transfer from source to sensor. While the extended source configuration has the limiting aperture at the detector, there is still room for error when conducting the setup for this measurement, so taking the time to set up the equipment correctly will bring more accurate results.

Measuring responsivity is very similar to the dark current measurement. First, the cryostat measurement test setup is fitted with equipment such as optical filters, optical choppers, and windows to keep the broadband infrared radiation from influencing the measurement. The cryostat is again cooled and the control sample temperature is set to 77K. The sample detector is biased with the trans-impedance amplifier (TIA) while receiving a sufficient gain from the TIA to strengthen the signal. The measurement is conducted with a network analyzer, and the measured photocurrents are processed using a MATLAB script to account for the measured relative spectral response, distance, detector area, blackbody temperature, sample temperature, etc. The responsivity results are plotted against voltage bias.

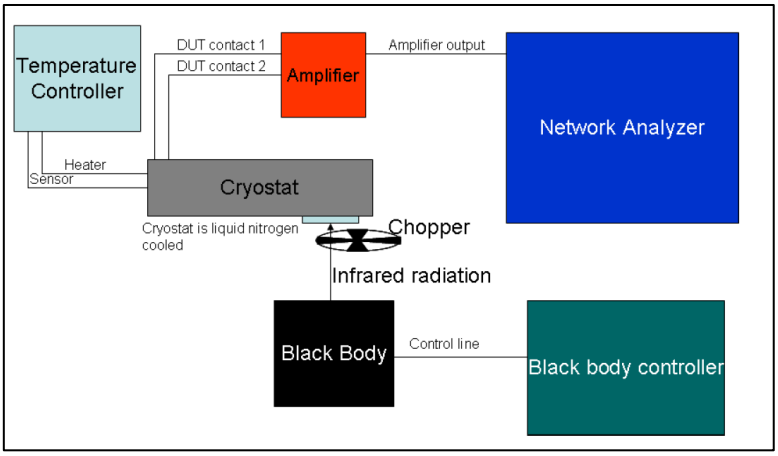

Figure 24: Responsivity Measurement Setup for Cryostat Test Setup [20]

The probe station test setup is similar to what was depicted for the cryostat research test setup with a couple of exceptions as seen in Figure 25. The detector still cools to 77K and is stabilized with a temperature controller, the chopping frequency stays at 400Hz, and the TIA still amplifies the signal. However, a lock-in amplifier replaces the network analyzer as the apparatus for collecting the photocurrent measurements. A notable difference is also the laser power source, which has the ability to pump 980nm laser light into a fiber optic to use as a radiation source for the responsivity measurement. Because it wasn't a blackbody like the other setup, this setup was deemed to not fit the scope of the research, therefore the measurement was only used for verification purposes.

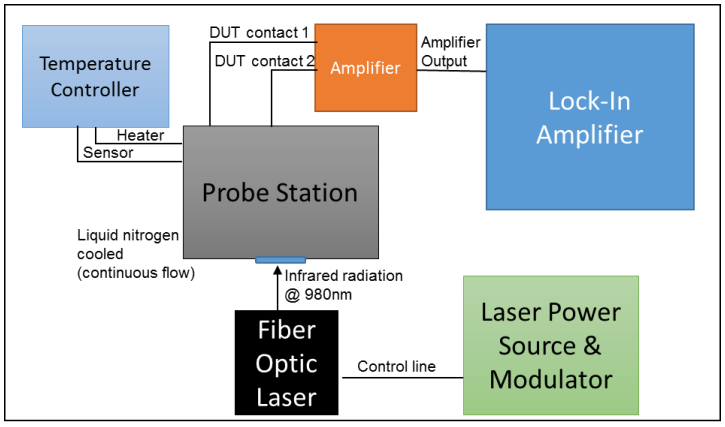

Figure 25: Responsivity Measurement Setup for Micro-manipulated Probe Station Test Setup

3.4 Quantum Efficiency

Quantum efficiency is the number of photons incident on the detector's active area to the number of independent electrons generated. The quantum efficiency is extracted from photocurrent measurements done using the responsivity measurement setup using the equation:

$$I_{photo} = \eta q A_{det} E_q$$

This parameter gives a percentage describing the efficiency of the conversion process of received photons to free electron hold pairs. [30] Again, this parameter was used to verify that the photocurrent was indeed different than the dark current measurements due to the responsivity measurement setups being dissimilar from one another.The results for both responsivity and quantum efficiency are reported in the results in Chapter 4.

3.5 Other Figures of Merit

Other Figures of Merit used for infrared detector characterization are noted here to complete the characterization of infrared detectors discussion. These Figures of Merit were not considered to be reportable results for this work because they were either irrelevant to single pixel detectors or immeasurable due to equipment and time constraints.

Detectivity is a calculated parameter that normalizes the detector sensitivity to a $1cm^2$ area detector and a 1Hz noise equivalent bandwidth. This is used for comparing on

a common baseline, however, the comparison in this research was between the test setups and not the detectors themselves. [9]

The Noise Current or NEP (Noise Equivalent Power) can be defined as the minimum radiant-flux level a detector can recognize due to its own noise level – meaning the input power must be above the noise current to be distinguished. [9] This measurement was not completed because of the unfamiliarity of the noise measurement setup and equipment necessary to complete the measurement in an accurate and viable manner.

Noise Equivalent Temperature Difference (NETD) of a detector represents the temperature change due to the incident radiation upon the detector where the output signal is equal to the root mean squared noise level. [31] Noise Equivalent Temperature Difference (NETD) was not considered because it is typically used for infrared focal plane arrays; this measurement is not typically used as a Figure of Merit for single pixel detectors because there is too much variance between each pixel to be able to compare this parameter accurately. NETD was also not considered because there is no difference between the array measurement and the single pixel measurement other than system noise influence such as ROIC noise. [31] This is especially irrelevant at the pixel level, because there are other factors of noise dominating the detector's performance found at the single pixel level that are not dominant on a larger scale array.

3.6 SUMMARY

This chapter presented the relevant Figures of Merit considered for measuring the single pixel mid-wave infrared strained-layer super-lattice materials being used for this project. For each Figure of Merit basic definitions were listed to help grasp each concept

including: 1) a brief description of the parameter's function and importance; 2) equations supporting the description; and 3) how the parameter was measured on each detector using the test setups described. It also touched on other Figures of Merit that are important to mention, however, were not measured or calculated for this research. The general arrangement of equipment used to test and measure the detector for both the cryostat research test setup and the micro-manipulated probe station test setup were presented as reference for the experimental setup of measuring each of these Figures of Merit. With the results from these Figure of Merit measurements performed by each of the test setups, we will be able to conclude how each setup performs and compare them with quantifiable data to prove how similar the micro-manipulated probe station is to the cryostat.

4 RESULTS & DISCUSSION

The two research test setups were compared using measurement data from two different mid-wave infrared detector samples. These samples were described in Chapter 2 as single pixel detectors with either a pin MWIR architecture or a pBn MWIR single architecture. Each of the samples were installed in no particular order into the first research test setup, characterized by measuring the I-V characteristics in both dark and illuminated conditions at incremented operating temperatures, then were measured again using the second research test setup. Multiple iterations of the experiment were conducted and all results proved to be consistent as each iteration was compared to one another. The results presented in this chapter are of the data collected during one iteration of the experiment, which included the series of radiometric measurements listed in Table 3. The physical test setup conditions between the two sample measurements were kept as consistent as possible to provide confidence the two measurements could be compared to one another without imposing caveat effects onto the results. This included critical items such as:

- Keeping control of the sample temperature using a temperature controller. The control temperature sensor was installed on the sample mount located as close as possible to the sample for precise temperature measurement. [10]
- Evacuating the research test setup to a low vacuum of at least $1x10^{-5}$ atm to provide a suitable environment for cooling the sample with liquid cryogens. [32]
- Documenting time between measurements to assure the sample temperature has stabilized after each temperature increment.

Great care was taken to complete each Figure of Merit parameter test in a similar process to preserve the integrity of the data. The physical sample structures were specifically chosen to be a secondary variable of the experiment, to observe the variations between different semiconductor mid-wave infrared detector structures using different research test setups. This allows each individual experiment done on one of the samples to be able to stand alone while still comparing the two research test setup results and performance.

The testing matrix in Table 3 was used to keep track of the radiometric measurements taken on each sample with each research test setup. It was also used to document the results.

Table 3. Radiometric Measurement Testing Matrix

	Sample A	**Sample B**
Probe Station	Dark Current (various temps) Responsivity (77K)	Dark Current (various temps) Responsivity (77K)
Cryostat	Dark Current (various temps) Responsivity (77K) Spectral Response (77K)	Dark Current (various temps) Responsivity (77K) Spectral Response (77K)

These detector measurements were chosen to display the sample results because they were simple and repeatable; however the results are focused on highlighting the dark current measurements. Dark current was measured for all test cases because dark current is the most fundamental measurement taken to determine the quality of an infrared detector and was treated as the key measurement to determine the quantifiable differences between the cryostat setup and the probe station setup. [9] The current-voltage

measurements were completed using the equipment specified in the Figures of Merit discussion of dark current for each of the research test setups.

While responsivity was measured as described in the Figures of Merit section, it was only used to verify the dark current measurements by giving confidence in the measureable difference between dark current and photo current. A long pass filter with a 2.5μm cutoff wavelength was used during the responsivity measurement to block a broadband measurement from occurring. The filter spectral response is shown in both sample spectral response plots in Chapter 2 - Figure 8 and Figure 11 to point out the effect of the filter on the sample spectral response during responsivity measurements. Spectral response was measured to also verify each sample was indeed responsive to the mid-wave region of the infrared spectrum as describe in Chapter 2. The resulting confirmation showed the measured photo current was much higher than the measured dark current, which was not an expected outcome. The other figures of merit measurements had expected outcomes where each sample's spectral response indicates the detector's operating region is in the mid-wave infrared with cutoff wavelengths equal to 5.1μm and 3.2μm respectively. The average responsivity and quantum efficiency results for the Cryostat research test setup at a bias of -0.5V show a responsivity of 2.3A/W for Sample A and 0.45A/W for Sample B; and quantum efficiency of 59% for Sample A and 22% for Sample B. These results were comparable to other measurements done using the same samples for other projects.

4.1 SAMPLE A RESULTS

4.1.1 Dark Current Density versus Temperature

For Sample A, the pBn detector dark current was measured versus bias voltage at a number of temperatures. Based off of the detector area, the dark current density was calculated and plotted versus voltage bias for each temperature. The dark current density can be calculated using the measured current and dividing it by the detector area, giving a unit of A/cm^2. The voltage bias range used for the I-V measurements covered from -2V reverse bias to +2V forward bias. The temperature range used for the I-V measurements extended from 77K to 295K (or room temperature) in increments of about 50 degrees Kelvin. Multiple detector sizes were measured on each of the variable area detector arrays. The device size length on Sample A indicates the individual device aperture size, which can be calculated as $(100\mu m \text{ side})^2 = 1x10^{-8}\mu m^2$ aperture area. For the sake of simplicity, only the $175\mu m^2$ aperture size dark current measurements are shown for the dark current density results displaying the various I-V curves at each temperature for Sample A. Results from both research test setups for the dark current density versus temperature can be found in Figure 26 and Figure 27.

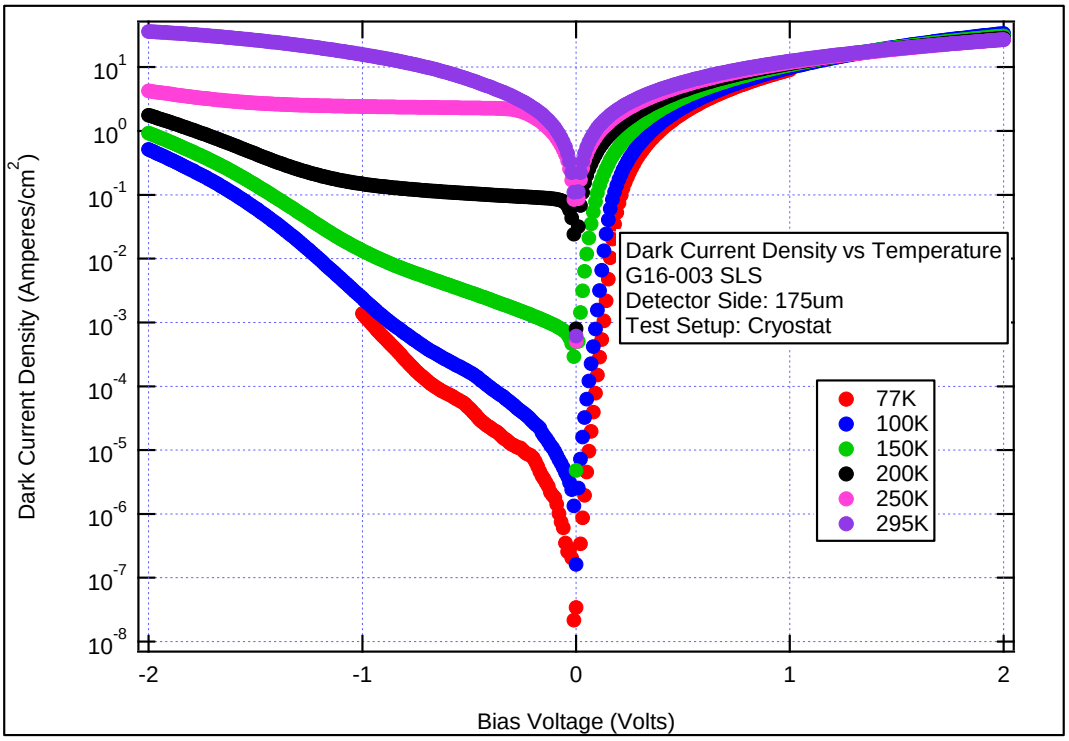

Figure 26: Dark Current Density versus Temperature of Sample A using the Cryostat Research Test Setup

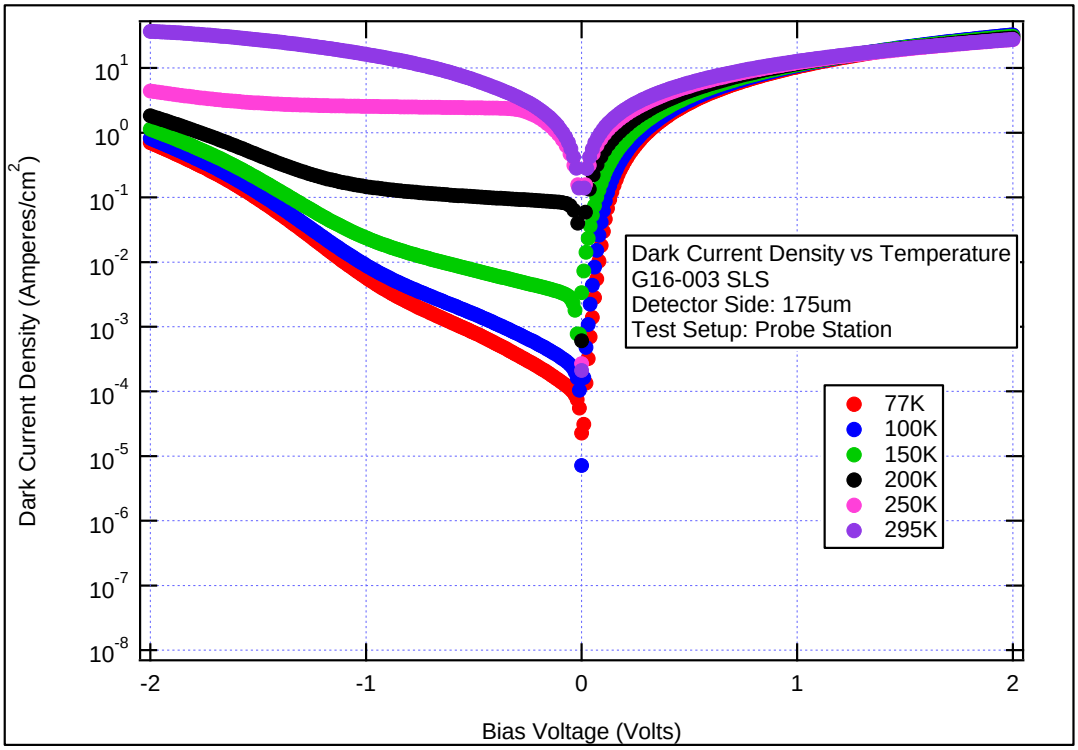

Figure 27: Dark Current Density versus Temperature of Sample A using the Probe Station Research Test Setup

The cryostat research test setup results show that the detector dark current for Sample A was reaching a minimum of about 50 nA/cm^2 at a near 0V bias voltage at a temperature of 77K. This reached up to a minimum dark current of 1mA/ cm^2 at room temperature. The probe station test setup results show that the detector dark current reached a minimum of about 10 µA/cm^2 near the 0V bias voltage at a temperature of 77K. This reached up to a minimum dark current of 0.7mA/ cm^2 at room temperature. Comparing the two minimums, we can observe immediately that there is a large difference between the two test setup measurements using the same sample.

4.1.2 Comparison of Dark Current Results

Comparing the dark current density measurements between the cryostat test setup and the probe station test setup, the dark current density data for Sample A trended perfectly between the two setups over the higher temperature current-voltage curves. The trend continued as the temperature decreased to 200K; but a discrepancy between the linearity of the data occurred between 200K and 150K. Figure 28 plots the two data sets over all temperatures up to 200K and includes a close-up image of the observed separation between them at 150K. This indicates that there is a measurable difference between the cryostat test setup and the probe station test setup due to the fact that both measurements were taken with the same testing parameters including the same sample structure – Sample A.

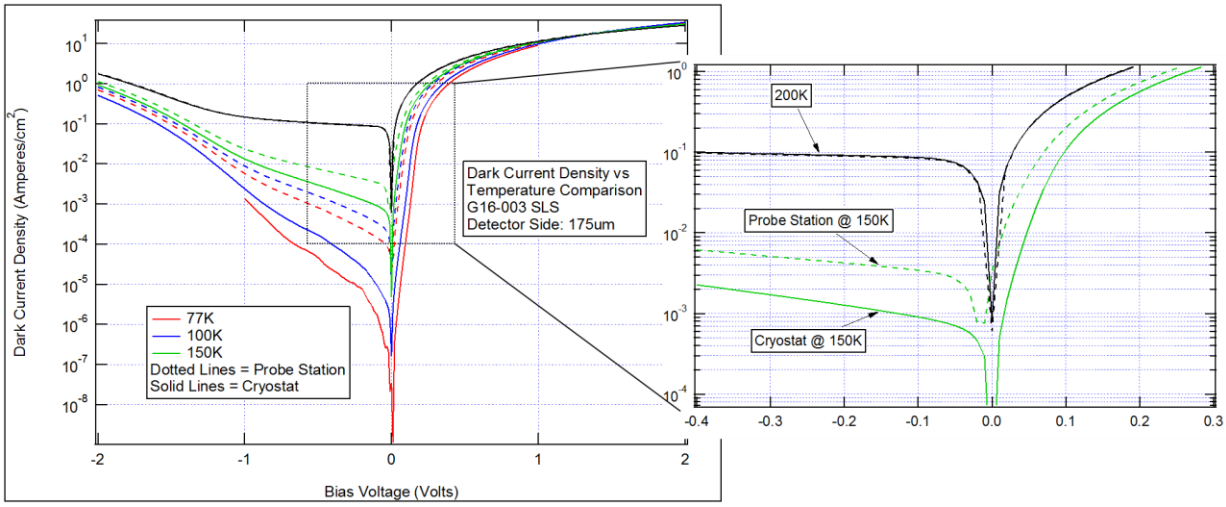

Figure 28: Comparison of Probe Station and Cryostat Dark Current Density versus Voltage Bias Sample A Results using Temperature Range from 77K to 200K. Separation of Dark Current Density between 150K data and 200K is plotted.

The current-voltage curves continued to show the separation as the temperature decrease to 77K. The characterization measurement results from the probe station test setup were not expected because the probe station test setup is claimed to have the ability to accurately measure dark current at such low temperatures. It was determined further investigation into why this might be occurring needed to be addressed. The second sample helped to answer this question by determining if this was a systemic issue with the probe station test setup or if it was an issue with the detector sample being used for these radiometric measurements.

4.2 Sample B Results

4.2.1 Dark Current Density versus Temperature

The pin detector dark current for Sample B was also measured at a number of temperatures exactly the same way as Sample A. The dark current density was again

calculated based off of the detector area size of the measured single pixel detector and was plotted versus each temperature. The temperature range used for the Sample B measurements extended from 77K to 295K (or room temperature) in increments of about 50 degrees Kelvin. The voltage bias used ranged from -2V reverse bias to +2V forward bias. Multiple detector sizes were measured, but only the 150µm dark current density measurements are shown to give a general outlook on the behavior of the dark current density of Sample B. I-V characteristic results from both research test setups for the dark current density versus temperature can be found in Figure 29 and Figure 30.

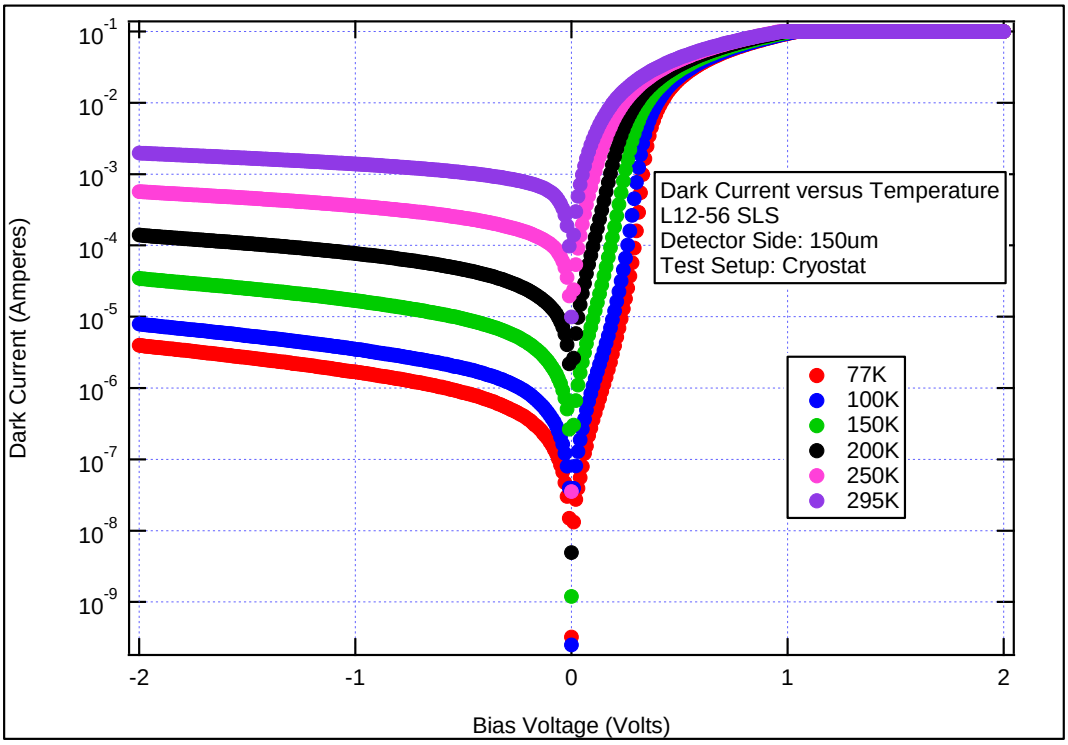

Figure 29: Dark Current Density versus Temperature of Sample B using the Cryostat Research Test Setup

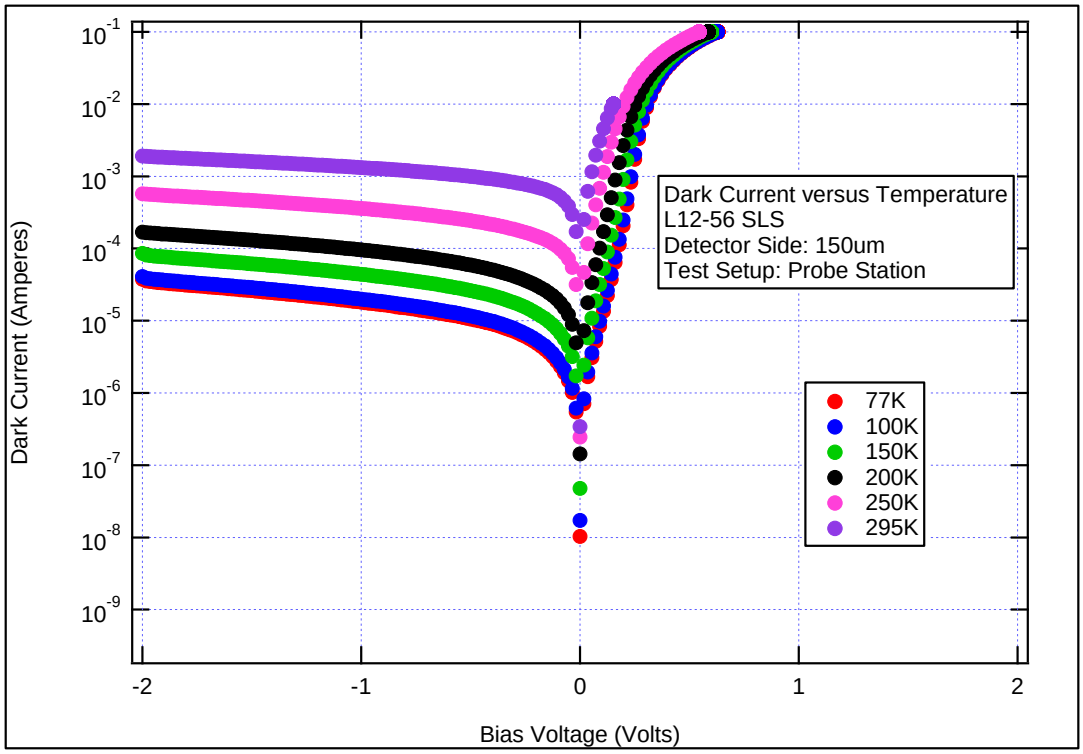

Figure 30: Dark Current Density versus Temperature of Sample B using the Probe Station Research Test Setup

The cryostat research test setup results show that the detector dark current for Sample B was reaching a minimum of about 10 nA/cm^2 at a near 0V bias voltage at a temperature of 77K. The probe station test setup results show that the detector dark current reached a minimum of about 1 µA/cm^2 near the 0V bias voltage at a temperature of 77K. This increased to a minimum dark current of 0.1mA/cm^2 at room temperature. Comparing the two minimums, we can again observe that the difference between the two test setup measurements using the same sample is large resulting in a two magnitude separation.

4.2.2 Comparison of Dark Current Results

For Sample B, the dark current density I-V characteristic measurements at different temperatures between the cryostat test setup and the probe station test setup were

compared resembling the previous comparison of the measurements from Sample A. The dark current density over the same temperature range between 77K and 200K showed a very similar outcome to the relationship discussed for Sample A. Again, the dark current density data trended similarly between the two setups over the higher temperature current-voltage curves for Sample B as well as Sample A. The trend continued as the temperature decreased to 200K and a discrepancy is observed between 200K and 150K as the two data sets were plotted together. Figure 31 plots the two data sets over all temperatures up to 200K and includes a close-up image of the observed separation at 150K. This suggests that there is also a similar measurable difference between the cryostat test setup and the probe station test setup using Sample B, which is a completely different structure than Sample A.

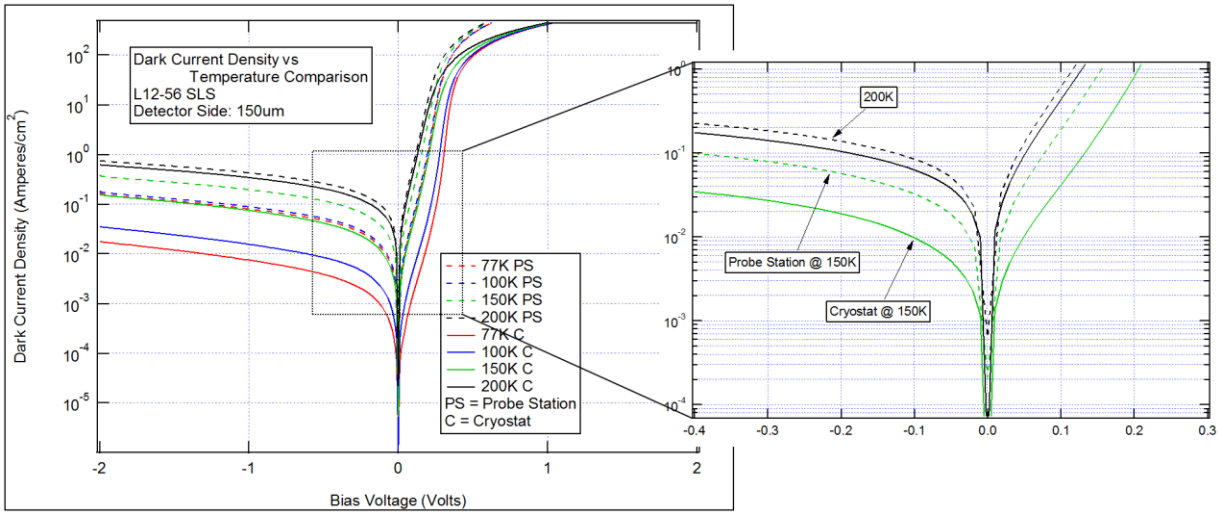

Figure 31: Comparison of Probe Station and Cryostat Dark Current Density versus Voltage Bias Sample B Results using Temperature Range from 77K to 200K. Separation of Dark Current Density between 150K data and 200K is plotted.

The current-voltage curves for Sample B continued to show the separation as the temperature decreased to 77K similar to the behavior seen in the Sample A results. An interesting phenomenon was discovered in the Sample B comparison plot between the

100K I-V curve and the 77K I-V curve. The 100K and 77K probe station dark current density I-V characteristic curves are almost identical to one other for a 25K temperature difference. According to the radiometry principles discussed earlier, the same current at two different temperatures is not possible and this could only mean that the sample temperature is the same for both of these I-V curve measurements. Recognizing the Sample B results echo the observations seen by the dark current density measurements in Sample A determines this inconsistency was a systemic issue with the probe station test setup while taking these radiometric measurements.

4.3 Results and Discussion of Low Temperature Dark Current

Below 150K, the dark current in the micro-manipulator probe station test setup was higher than the cryostat test setup. There are two possible explanations for the discrepancy in the dark current. One theory points to the background illumination in the probe station, and the other theory is inadequate thermal contact causing a thermal offset. After completing some diagnostic measurements, it was found that the cause of the discrepancy was the thermal offset between the micro-manipulator probe station sample mount temperature and the temperature of the LCC carrying the sample. This could be occurring because of a mismatch of coefficient of thermal expansion (CTE) that led to the delamination of the LCC from the sample mount due to the inadequate thermal contact between the two surfaces because of improper mounting techniques.

The evidence collected to determine the cause of this separation was completed with an additional temperature study to elucidate the discrepancy between the cryostat test setup and probe station test setup. The temperature study consisted of installing Silicon

temperature sensor diodes in three key locations within each test setup to monitor the surface temperature as the entire test system was cooled with the appropriate cryogens. The standard Silicon temperature sensor diodes purchased from Lake Shore Cryotronics were placed in the following locations:

- Shield Temperature – On the surface of the test setup inner shield, which is the shield around the sample creating the inner chamber.
- Sample Mount Temperature – On the sample mount, which is also the same location as the temperature sensor being sampled by the feedback loop of the temperature controller PID for sample temperature control.
- Sample Temperature – On an LCC simulating the location of the sample.

The temperature sensors installed in the sample mount and shield locations used mounting techniques such as: adding thermal grease between the diode and the surface, fastening the diode to the surface with a screw and washer, and wrapping the diode in aluminum foil tape to promote thermal contact with the surface being measured.

For the sample location, the diode needed to simulate the location of the sample. An image of the temperature sensor installed on the LCC is shown in Figure 32(a). The pictured LCC is the same LCC used to mount and carry the detector samples previously described in Chapter 2. The Silicon temperature sensor was mounted onto the LCC with silver epoxy to permanently affix it in the same manner as the sample mounting scheme. The bobbin packaged Silicon temperature sensor has four connecting wires, two on the anode side and two on the cathode side of the diode, as seen in Figure 32(b) to separate the current and voltage electrodes to reduce the contact resistance from the measurement, thus making a more accurate resistance measurement. [33] The temperature sensor uses

the DT-670 standard voltage versus temperature response curve provided by Lake Shore Cryotronics to interpret the voltage to temperature conversion in the temperature controller to report the correct temperature result. [33]

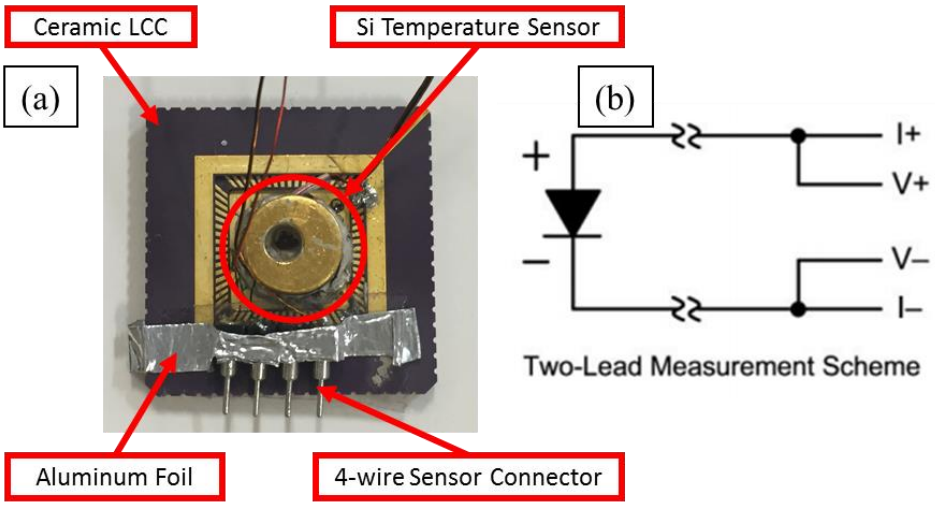

Figure 32: (a) KYOCERA 68-pin LCC with Silicon Temperature Sensor Bobbin Installed using Silver Epoxy (b) Schematic of Silicon Temperature Sensor Two-Lead Measurement Scheme using 4-wire Sensor Connector

The Silicon temperature sensor diodes were directly measured by two types of temperature controllers, a Lake Shore Cryotronics 330/331 Temperature Controller and a Scientific Instruments 9700 Temperature Controller. The LCC with the temperature sensor installed on it would be installed in each test setup like the sample was installed. The LCC temperature sensor was functionally validated by reading the temperature on the temperature controller when the sensor was connected to the temperature controller. The test setup was closed and evacuated to the proper atmosphere and the temperature sensors were validated one more time. The measurement then started by taking data from all three sensors with a GoPro camera every five minutes or manually every three minutes while the test setup is cooling. The resulting data for both test systems are found in sections 4.3.1 and 4.3.2.

4.3.1 Thermal Cycling Results of Cryostat Research Test Setup

For the cryostat test setup, the test process described in the previous section was used to conduct the cool down procedure for the temperature study. The Silicon temperature sensor diodes were measured using the two Lake Shore Cryotronics Temperature Controllers, model numbers 330 and 331. The LCC with the temperature sensor installed on it was installed in the LCC sample holder according to the Figure 33.

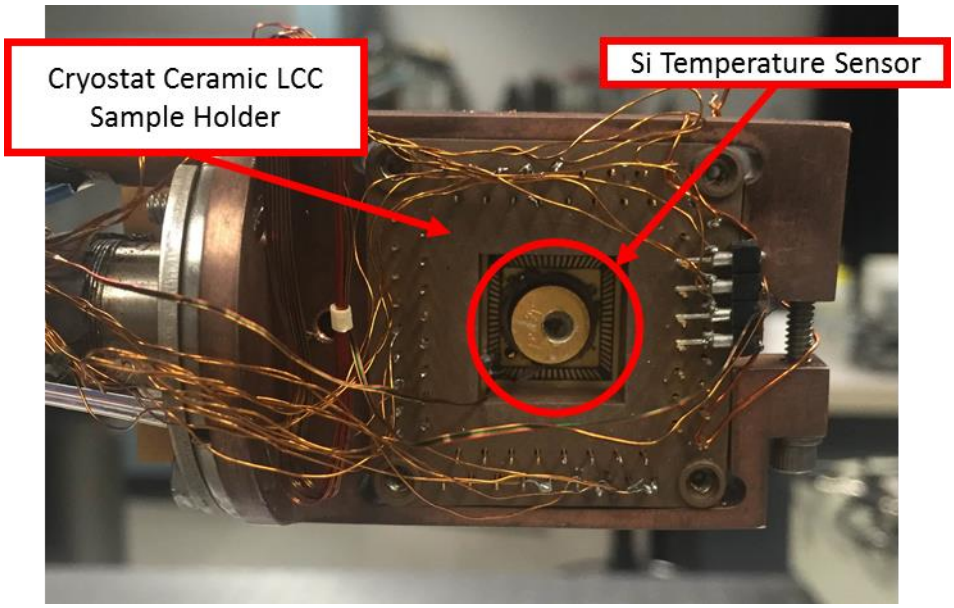

Figure 33: KYOCERA 68-pin LCC with Silicon Temperature Sensor Bobbin Fastened into Cryostat Test Setup LCC Holder and Sample Mount

The test setup was closed and evacuated to the proper atmosphere and the temperature sensors were validated before commencing the cool down of the cryostat test setup. Data was taken from all three sensors manually (by hand) every three minutes while the test setup cooled down until the 77K sample temperature was reached.

The results for the cryostat research test setup temperature study are presented as a plot showing temperature versus time in minutes in Figure 34.

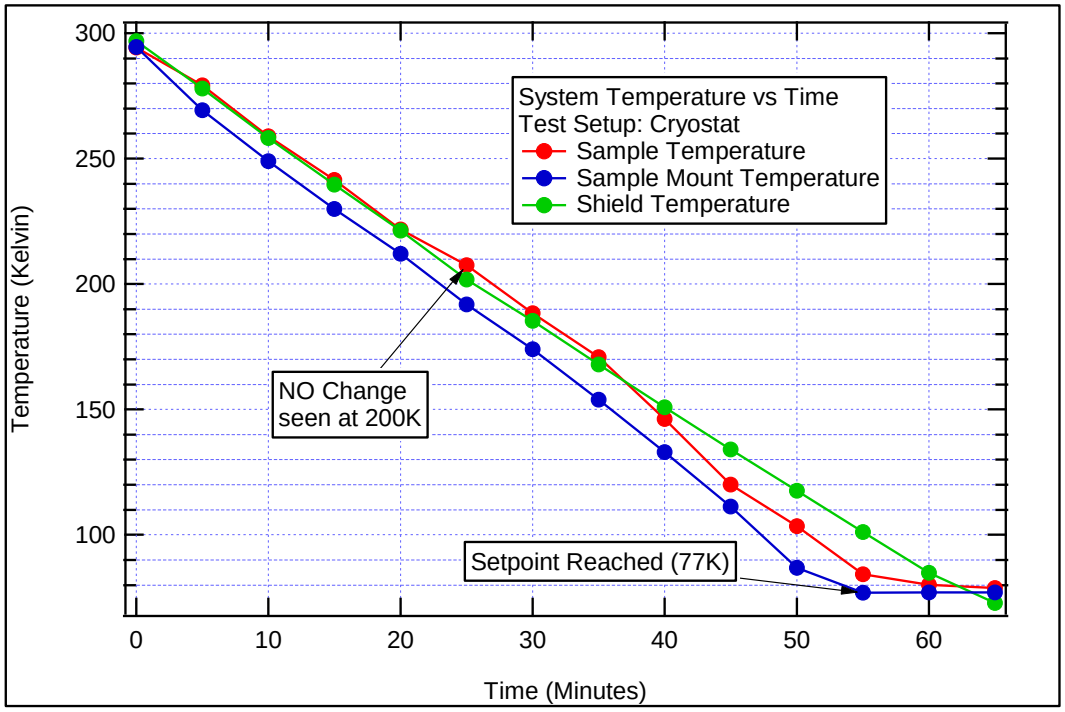

Figure 34: Cryostat Research Test System Cool Down Temperature Measurement Over Time. Observed Normal Behavior for All Surfaces.

As expected, the temperature results show all locations within the cryostat test setup are cooling at the same rate with the closed-cycle LHe compressor being used to cool the sample mount and shield. The sample temperature reached the setpoint temperature of 77K within an hour, thus showing that the cryostat cool down behavior is normal. [23] Another note to point out, the temperature of the sample LCC quickly reached the same temperature as the sample mount and stayed close to the sample mount temperature as it settled to the setpoint temperature of 77K. This evidence brings confidence that the epoxy holding Silicon temperature sensor succeeded in keeping the temperature sensor fastened onto the LCC as the unit was cooled, thus ruling out the epoxy being a possible surface where the separation is occurring.

4.3.2 Thermal Cycling Results of Probe Station Research Test Setup

The micro-manipulated probe station test setup went through several temperature cool down/warm up cycles to document the behaviors observed in the temperature data. Like the cryostat test setup, the test process described in the previous section was used to conduct the cool down procedure for the temperature study. The Silicon temperature sensor diodes were measured using the same Lake Shore Cryotronics 330 Temperature Controller for the LCC sample temperature sensor from the cryostat test setup measurement as well as the Scientific Instruments 9700 Temperature Controller for the other two temperature sensor diodes. The LCC with the temperature sensor installed on it was placed on the LCC sample holder according to Figure 35 as the equivalent configuration used during the dark current measurements.

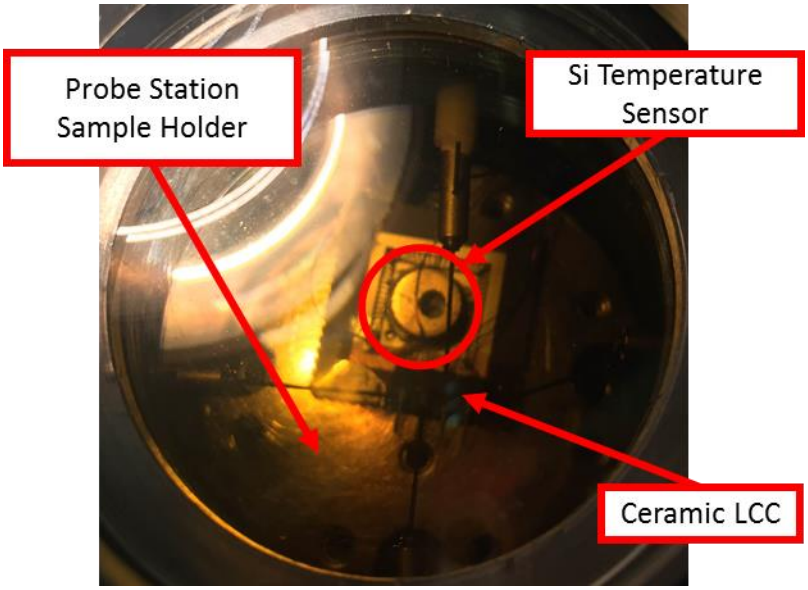

Figure 35: KYOCERA 68-pin LCC with Silicon Temperature Sensor Bobbin Installed on the Probe Station Test Setup Sample Mount using Thermal Grease

The test setup was closed and evacuated to the proper atmosphere and the temperature sensors were validated before starting the cool down of the probe station test

setup. Data was taken from all three sensors with a GoPro camera every five minutes while the test setup cooled down. Temperature results show the probe station was cooling overall as a system, however, the sample temperature never reached the 77K setpoint temperature. Therefore, the measurement was taken as long as possible to show what the sample temperature was able to reach in the time frame of the study.

The overall results for the probe station test setup temperature study are presented as a plot showing temperature versus time in minutes in Figure 36 depicting a full thermal cycle of the probe station test setup. Interestingly enough, the probe station test setup did not follow the normal linear cool down behavior like the cryostat test setup did.

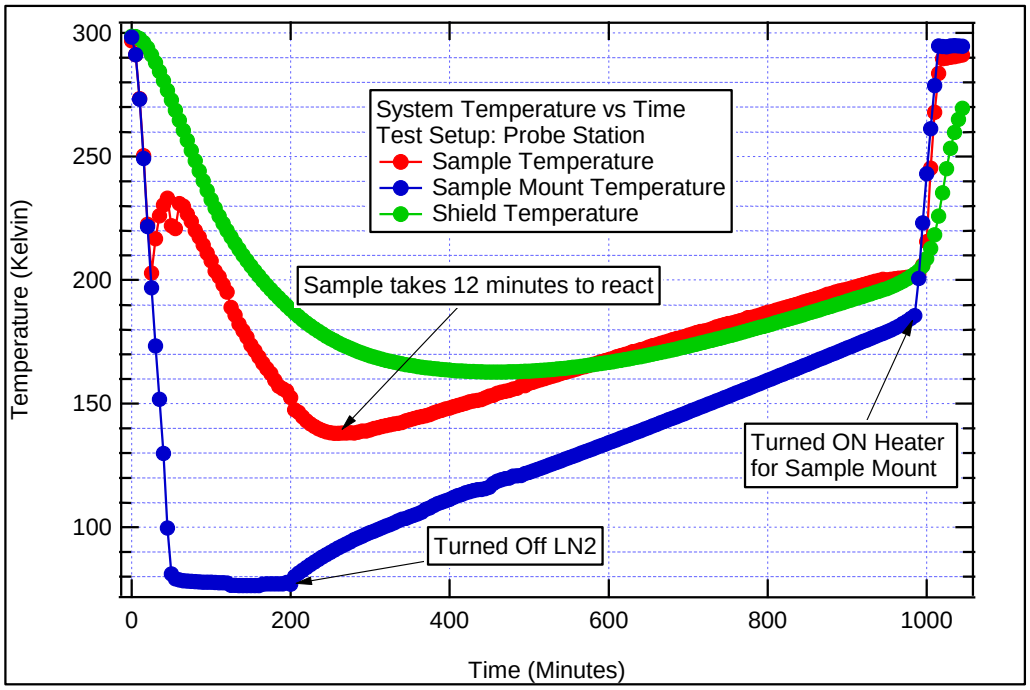

Figure 36: Full Temperature Cool Down and Warm Up on Probe Station Test Setup

A zoomed in plot of the cool down period of the temperature study shown in Figure 37 give some hints as to what is occurring during the cool down of the probe station test setup. As the system is cooled with the continuous flow of liquid nitrogen (LN2), typical

cool down physical attributes seen during large cryogenic Dewar cool down measurements are observed between the sample, sample mount, and the shield. [34] The sample mount is directly cooled with the LN2 through the reservoir port, making it the fastest object being cooled in the system. The sample temperature should, and does, follow closely behind the sample mount temperature because the sample mount is usually the closest place to the sample being probed for temperature measurement and control to reference the sample's temperature non-invasively. The shield trails behind the other two temperature locations because the shield is a larger thermal load for the LN2 to accommodate. What is different from typical cool down curves is the change in sample temperature seen at the "Change #1" marker at 200K on Figure 37. The sample temperature starts to increase sharply at about 200K while the rest of the system continues to decrease in temperature. After 230K, the sample temperature plateaus and starts to decrease with a new yet similar slope parallel to the shield temperature slope or rate.

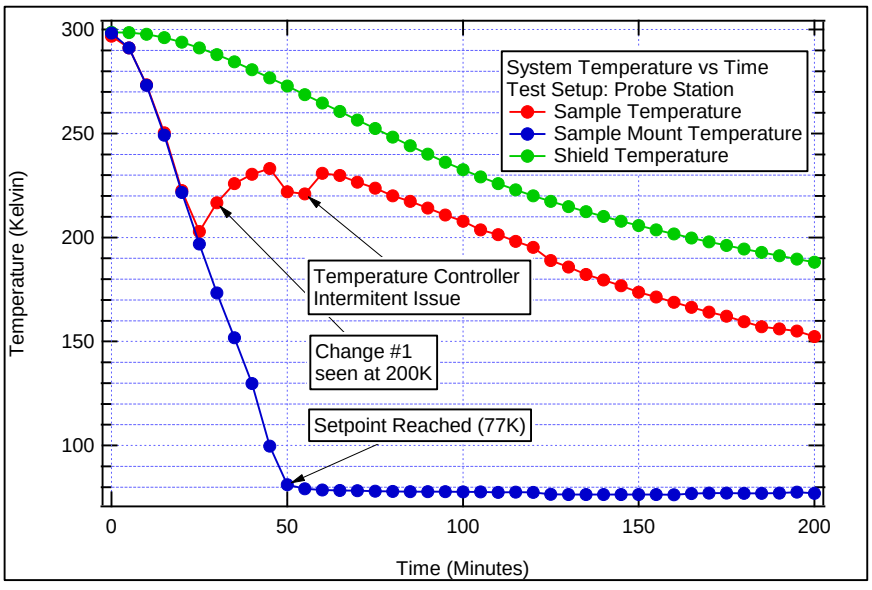

Figure 37: Probe Station Test Setup Cool Down Where Delamination Occurs at 200K

According to literature, a simple explanation for this event could be the result of a thermodynamics principle called heat transfer. Heat transfer utilizes the first law of thermodynamics, which states that energy can neither be created nor destroyed, only converted from one form to another, to describe the transfer of thermal energy between systems. [35] Multiple modes of heat transfer could be occurring during the cool down process such as conduction, convection, or radiation. [35] However, in order to understand if this temperature measurement was not a singular event and a result of heat transfer traits, the probe station test setup temperature needed to be monitored again to determine if the event stays consistent and repeatable.

This drastic temperature change can be seen in a repeated measurement as shown in Figure 38 with a similar temperature increase at 200K. In fact, several changes were observed during the second cool down measurement pointed out by “Change” markers on Figure 38. While the simple heat transfer theory would suffice for the first case at “Change #1”, other cases within the curve would need more complex explanation due to the number of variables possibly influencing the curve behavior due to thermodynamics theory. Nonetheless, the overall trend between the two measurement iterations shows that there is a thermodynamic heat transfer occurring at a point around a system temperature of 200K where the sample temperature shows that there is a thermal influence on the sample that has changed it from a conductive heat transfer mode to a convective heat transfer mode.

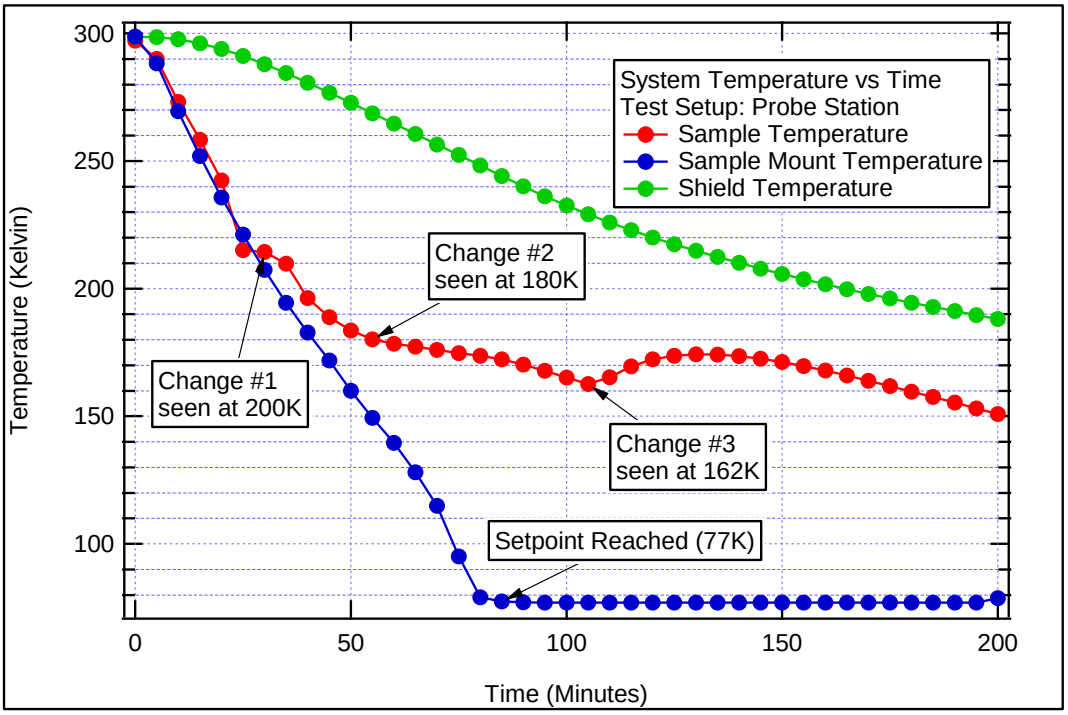

Figure 38: Probe Station Test Setup Cool Down Measurement #2

When the sample starts being cooled, the slope between the sample temperature and the sample mount temperature are the same – this region could be labeled as conductive heat transfer because the two surfaces are influencing one another as they vibrate against one another's neighboring particles due to thermal contact. Conduction heat transfer is the most common method of heat transfer between solid objects in thermal contact. [35] The slope then changes at the point of interest, which could indicate that the mode has moved to convective heat transfer due to some change in the system. The system change could be that the two surfaces are no longer able to influence one another because they are no longer in good thermal contact. Thermal contact between the sample mount and the sample LCC surfaces is a key point in the system setup of the probe station as seen in **Error! Reference source not found.** because the main cooling method of the sample is

subjected to being in direct contact with the surface of the sample mount that is being cooled by the liquid nitrogen.

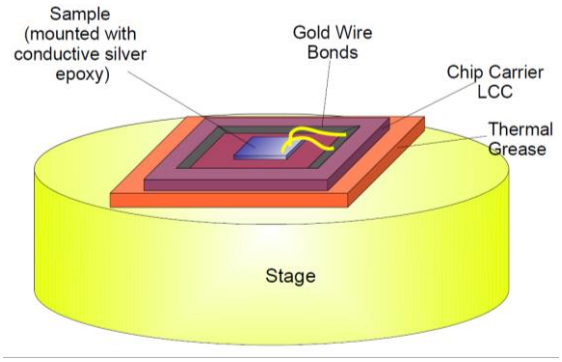

Figure 39: Cartoon Depicting the LCC Surface and the Probe Station Sample Mount Surface During Cool Down

Thus the heat flow between the two objects needs to be studied – known as the thermal contact conductance. [36] When two surfaces share an interface, the heat flow is directly related to the thermal conductivities (ability to conduct heat) of the two systems in contact by defining the heat transfer or heat flow as:

$$q = -kA\frac{dT}{dx}$$

q = heat flow

k = thermal conductivity

A = cross-sectional area

$\frac{dT}{dx}$ = temperature gradient in the direction of flow

Taking a close look at the equation, the heat flow is directly related to the thermal conductivities of the surfaces in contact. [36] Since the thermal conductivities are constants defined by the material properties of the two surfaces in thermal contact, the

linearity of the data can be related to these constants to show there is a possibility for the two surfaces to become disconnected from one another, losing the thermal contact needed to stay at the same temperature.

The material properties for the sample LCC and the probe station test setup were located in documentation pertaining to each system to make the comparison previously discussed. The thermal conductivity for ceramic leadless chip carriers used for mounting the samples used in this experiment is 14 W/mK. [25] The coefficient of thermal expansion (CTE) for ceramic leadless chip carriers used for mounting the samples used in this experiment is 7.1ppm/K (parts per million/Kelvin). [25] Examining the sample mount on the probe station test setup, the mount is made of solid copper with a nickel-gold alloy plating coating the copper, commonly called electroplated copper. The thermal conductivity for this particular setup is about 450 W/mK [37] while the coefficient of thermal expansion is well-defined at 15ppm/K because it is a very common material. [38] We can see that the difference in thermal conductivity and coefficient of thermal expansion for each of these materials is grossly mismatched, giving evidence that the systemic temperature changes between them while in thermal contact could shift them to disconnect after enough of a gap in between the two temperatures has occurred.

One element in the thermal system stack up that needs to be mentioned is the thermal grease located in between the sample and the sample mount in the Figure 39 for the probe station test setup. The sample was installed onto the probe station sample mount using only thermal grease called Apiezon N Grease as pictured in Figure 19. [39] Apiezon N Grease is a thermally conductive grease (thermal conductivity of +300 W/mK) that can perform well at very low temperatures, such as LN2. Therefore we can view the thermal

grease as an extension of the high thermal conductivity of the sample mount in the system stack up because they are similar in thermal conductivity. However, according to literature findings the N Grease is pliable at room temperature, but solidifies at cryogenic temperatures. Grease solidification is claimed to allow for easy mounting and removal of sensors, but it does not say if there is an adequate amount needed for assurance the grease will not separate from surfaces during the solidification process. [39] There is a possibility that the amount of applied thermal grease is more important than previously thought where not enough thermal grease without the proper clamping of the sample could degrade the thermal contact by separating the two surfaces instead of holding them together in good thermal contact.

No metallic tabs or screws were used to keep the sample in good thermal contact with the sample mount. Not fastening the sample down to the mount allowed for a thermodynamic mechanism called delamination to affect the physical connection between the sample and the sample mount shown in **Error! Reference source not found.**. Delamination is described as the failure mode in which two surfaces once in good thermal contact became separated due to a large change in temperature between the two surfaces. [40] The point of interest indicated as “Change #1” in Figure 37 and Figure 38 where the heat transfer mode changes can be called the delamination point. The delamination seen in the temperature measurements can be claimed as main conclusion using the accumulated evidence as to why the dark current measurements taken with the probe station test setup were higher than the dark current measurements taken with the cryostat research test setup.

Once the heat transfer change of the system was identified as the delamination of the sample LCC from the sample mount surface, further measurements were conducted to prove that the separation can be prevented so that the thermal contact of the two surfaces stays connected. The most recent cool down measurements taken on the probe station are presented in Figure 41.

The temperature measurement was conducted as previously described for the probe station test setup with one exception – the sample LCC was fastened to the sample mount as depicted in Figure 40Figure 41. The temperature of the sample, sample mount and shield were taken. The temperatures of the probe station test setup were not monitored for as long as the previous measurement, but the cool down was monitored until the sample mount temperature reached the setpoint of 77K.

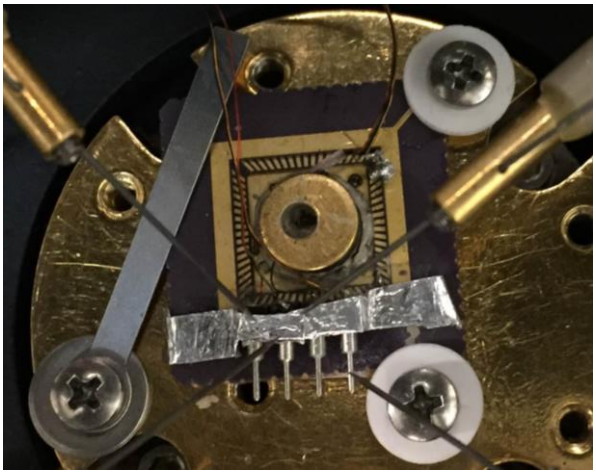

Figure 40: LCC installed in Probe Station with fastener washers and screws

The LCC fastener configuration shown in Figure 40 kept the LCC in good thermal contact with the sample mount and caused a similar result in the probe station test setup that was previously illustrated in the cryostat measurement data given in Figure 34.

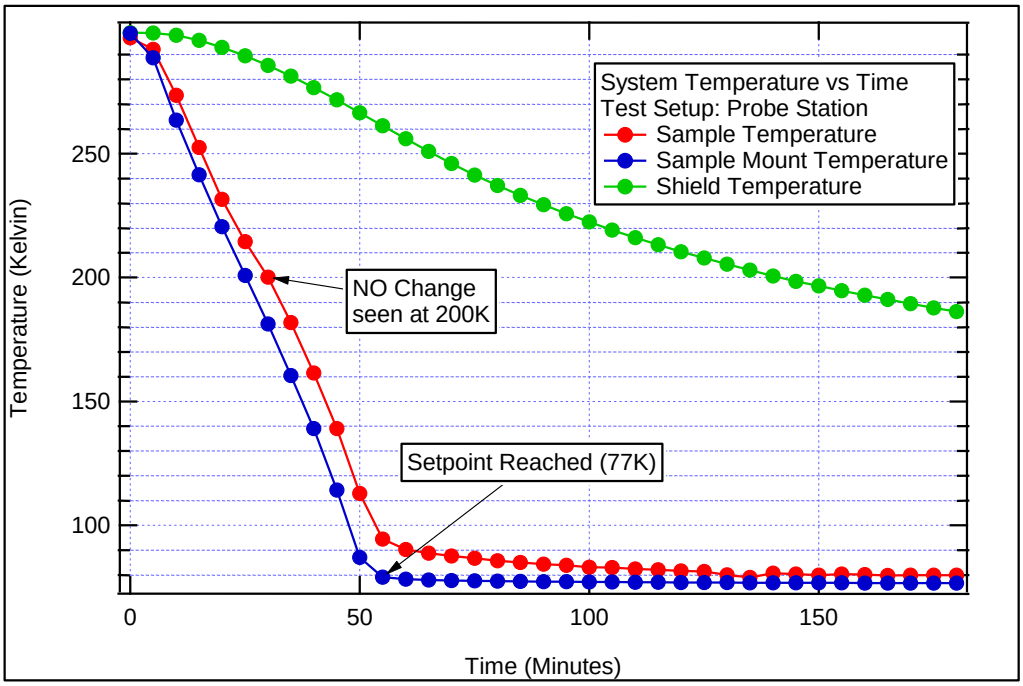

Figure 41: Temperature Cool Down with LCC Fastened to Sample Mount

This proves that the delamination between the sample LCC and the sample mount did occur and can be mitigated through proper fastening of the sample to the sample mount.

4.4 Conclusions

It has been demonstrated through this research that wafer level integration is possible using a probe station measurement technique on photodetectors. This was demonstrated at higher operating temperatures of 150K to 300K by comparing the performance of two different strained-layer super-lattice mid-wave infrared (3-5.5 µm) photonic detectors using a conventional cryostat research test setup and a micro-manipulator probe station test setup. The detectors were radiometrically characterized using each system to benchmark their performance in these two systems.

The measured dark current results show that the micro-manipulated probe station test system is quantifiably similar to the cryostat research test system; however below150K, the dark current in the micro-manipulator probe station test setup was higher than the cryostat test setup. It was determined that inadequate thermal contact between the sample LCC and the sample mount in the probe station test setup caused a delamination point between the two surfaces, thus creating a higher temperature result in the dark current measurements. To ensure thermal contact, fastening the LCC to the sample mount would improve the probe station performance to be similar to the cryostat at temperatures below 150K.

Because the probe station is designed to characterize detector material without tedious wirebonding and expensive leadless chip carrier waste, we can conclude it can be used to characterize detectors at the wafer level providing a higher throughput compared with a traditional cryostat. This work will allow future detector characterization to be completed using a probe station instead of a traditional cryostat test system, thereby reducing the test and measurement time for infrared photon detectors.

4.5 Future Work

The probe station was not able to viably measure baseline radiometric measurements down to a temperature of 77K for this thesis due to the background temperature dependence of the sample's delamination from the sample mount. Proving a mitigation method to solve the delamination problem gives the ability to overcome the demonstrated temperature constraints in the radiometric measurements and lower the baseline temperature further to 77K for radiometric measurements in the probe station test setup.

For example, measuring the dark current again with thermal strapping of the LCC to the sample mount can be repeated to quantitatively prove the full temperature range can be achieved.

Additional improvements to the probe station setup are being considered as an opportunity to bring the ability to take reliable responsivity measurements with a fiber coupled laser that operates in the mid-wave infrared region. This will be implemented and tested to further characterize photon detectors for quality performance at the wafer level.

Future research opportunities can be investigated once these improvements are implemented to bring a higher functioning system up to characterize photon detectors. For example, the developed system could eventually characterize photon detectors to determine how raise the operating temperature of these mid-wave infrared photon detectors. By using the radiometric measurements at the research and development level, those results can be used to optimize the quality assurance processes in factory settings and eventually complete the commercialization of these detectors for future applications in the infrared detector community.

5 REFERENCES

[1] P. Kruse and D. Skatrud, Uncooled Infrared Imaging Arrays and Systems, Academic Press, 1997.

[2] FLIR, "The World's Sixth Sense," FLIR Systems, Inc., 2016. [Online]. Available: http://www.flir.com/wss/. [Accessed May 2016].

[3] P. Kruse, "A comparison of the limits to the performance of thermal and photon detector imaging arrays," *Infrared Physics & Technology*, vol. 36, no. 5, pp. 869-882, August 1995.

[4] J. Keller, "DARPA launches WIRED program to develop affordable wafer-scale infrared sensors," *Military and Aerospace Electronics*, 11 September 2015.

[5] NASA JPL, "Development of Technologies Based on III-V Compound Semiconductor Heterostructures Continues," NASA Jet Propulsion Laboratory (JPL), California Institute of Technology, 2015. [Online]. Available: http://microdevices.jpl.nasa.gov/capabilities/infrared-photodetectors/compound-semiconductor-heterostructures.php. [Accessed May 2016].

[6] NASA JPL, "Infrared Detectors: Dual-band Megapixel QWIP FPAs," NASA Jet Propulsion Laboratory (JPL), 2008. [Online]. Available:

http://microdevices.jpl.nasa.gov/capabilities/infrared-photodetectors/qwip-fpas.php. [Accessed July 2016].

[7] V. Koifman, "News and discussions about image sensors," Image Sensors World, October 2011. [Online]. Available: http://image-sensors-world.blogspot.com/2011_10_01_archive.html. [Accessed July 2016].

[8] Wikimedia Commons, "EM Spectrum," 2007. [Online]. Available: https://commons.wikimedia.org/wiki/File:EM_spectrum.svg. [Accessed May 2016].

[9] E. L. Dereniak and G. D. Boreman, Infrared Detectors and Systems, John Wiley & Sons Inc., 1996.

[10] J. D. Vincent, S. E. Hodges, J. Vampola, M. Stegall and G. Pierce, Fundamentals of Infrared and Visible Detector Operation and Testing, 2nd ed., Wiley, 2016.

[11] C. A. Balanis, Advanced Engineering Electromagnetics, John Wiley & Sons, Inc., 2012.

[12] Protherm, "Infrared Basics," 2013. [Online]. Available: http://www.pro-therm.com/infrared_basics.php. [Accessed May 2015].

[13] American Technologies Network, "Night Vision Technology: How Night Vision Works," ANT Corporation, 2016. [Online]. Available: https://www.atncorp.com/hownightvisionworks. [Accessed July 2016].

[14] J.-M. Liu, Photonic Devices, Cambridge: Cambridge University Press, 2005.

[15] D. F. Welch, "A brief history of high-power semiconductor lasers," *IEEE Journal of Selected Topics in Quantum Electronics,* vol. 6, no. 6, pp. 1470 - 1477, 2000.

[16] M. J. Cantella, "Space Surveillance with Medium-Wave lrifrared Sensors," *The Lincoln Laboratory Journal,* vol. 1, no. 1, pp. 75-88, 1988.

[17] Wikimedia Commons, "File:Atmosfaerisk spredning.png," 2014. [Online]. Available: https://commons.wikimedia.org/w/index.php?curid=34818020. [Accessed May 2016].

[18] M. Aggarwal, A. Batra, P. Guggilla, M. Edwards, B. Penn and J. Currie Jr., "Pyroelectric Materials for Uncooled Infrared Detectors: Processing, Properties, and Applications," National Aeronautics and Space Administration (NASA) - Marshall Space Flight Center, Alabama, 2010.

[19] InfraTec Infrared LLC, "Snesor Division Knowlege: Pyroelectric Detectors," InfraTec Infrared LLC, 2016. [Online]. Available: http://www.infratec-infrared.com/sensor-division/sensor-division-knowledge.html. [Accessed July 2016].

[20] D. S. Myers, "Mid-Wave and Long-Wave Single Uni-polar Barrier Infrared Detectors Based on Antimonide Material System," 2013.

[21] D. R. R. (NIST), "NIST Cryogenic Technologies Group: About Cryogenics," *The MacMillan Encyclopedia Of Chemistry,* 2002.

[22] A. Jeromen, "Dewar Vessel," 2000. [Online]. Available: http://fizika.imfm.si/jeromen/piscal/dewar-a.html. [Accessed May 2016].

[23] Janis Research Company, LCC, "Products - VPF Series Cryostat Systems - Sample in Vacuum," 2015. [Online]. Available: http://www.janis.com/LN2_Home_KeySupplier.aspx. [Accessed April 2016].

[24] Spectrum Semiconductor Materials, Inc. , "KYOCERA Corporation A-440 Leadless Chip Carrier".

[25] KYOCERA Corporation, "Ceramic Products: Material Properties," [Online]. Available: http://global.kyocera.com/prdct/semicon/material/ . [Accessed June 2016].

[26] Janis Research Company, LLC, "Products - Micro-manipulated Cryogenic & Vacuum Probe Systems for Chips, Wafers and Device Testing from ~3.5 K to 675 K," 2015. [Online]. Available: http://www.janis.com/Products/productsoverview/MicromanipulatedProbeStations.aspx. [Accessed April 2016].

[27] D. A. Neamen, Semiconductor Physics and Devices: Basic Principles, 3rd ed., McGraw-Hill, 2003.

[28] ThermoNicolet, "Introduction to Fourier Transform Infrared Spectrometry," ThermoNicolet Corporation, Madison, WI, 2001.

[29] ThermoFisher Scientific, "Fourier Transform Infrared (FTIR) Spectroscopy," ThermoFisher Scientific Inc., 2016. [Online]. Available: https://www.thermofisher.com/us/en/home/industrial/spectroscopy-elemental-isotope-

analysis/molecular-spectroscopy/fourier-transform-infrared-ftir-spectroscopy.html. [Accessed February 2016].

[30] S. Kasap, Optoelectronics and Photonics: Principles and Practices, Upper Saddle River: Prentice Hall, Inc., 2001.

[31] C. DeCusatis, V. Lakshminarayanan, C. Macdonald, C. DeCusatis, G. Li, V. Mahajan, E. Van Stryland, M. Bass and J. Enoch, "Infrared Detector Arrays," in *Handbook of Optics: Design, Fabrication and Testing, Sources and Detectors, Radiometry and Photometry*, 3rd ed., vol. II, McGraw-Hill Education, 2009.

[32] M. Jirmanus Ph.D., "Introduction to Laboratory Cryogenics," Janis Research Company, Inc., Wilmington, MA, 2009.

[33] Lake Shore Cryotronics, Inc., "Instructions, Silicon Diode Temperature Sensor Installation, Model DT-470, 471, 670, and 671 BO Packages," Lake Shore Cryotronics, Inc., 2016. [Online]. Available: http://www.lakeshore.com/Documents/F008-00-00.pdf. [Accessed July 2016].

[34] T. Specht, "Infrared Radiation Effects Laboratory Large Dewar Cool Down Study," Internal Report: Ball Aerospace, Albuquerque, 2014.

[35] J. Abbott, H. Smith and M. Van Ness, Introduction to chemical engineering thermodynamics (7th ed.), Boston: McGraw-Hill, 2005.

[36] C. Madhusudana and F. Ling, Thermal Contact Conductance, Springer, 1995.

[37] R. Powell, C. Ho and P. Liley, "Thermal Conductivity of Selected Materials," National Standard Reference Data Series - National Bureau of Standards -US Dept. of Commerce, Washington, D.C., 1966.

[38] ASM International, "Thermal Expansion," in *ASM Ready Reference: Thermal Properties of Metals*, Materials Park, OH, ASM International , 2002, pp. 9-13.

[39] M&I Materials Ltd. , "Apiezon N Grease and Cryogenics," M&I Materials Ltd. , 2016. [Online]. Available: http://www.apiezon.com/products/applications/cryogenics. [Accessed July 2016].

[40] D. L. Summers, Advances in Cryogenic Engineering Materials, Columbus: Springer Science+Business Media, LLC, 1997.

[41] D. B. Klein, "Defect Investigations in InAs/GaSb Type-II Strained Layer Supperlattice," 2014.

[42] S. Myers, E. Plis, C. Morath, V. Cowan, N. Gautam, B. Klein, M. N. Kuttya, M. Naydenkova, T. Schuler-Sandya and S. Krishna, "Comparison of superlattice based dual color nBn and pBp infrared detectors," in *SPIE - The International Society for Optical Engineering*, 2011.

[43] T. Schuler-Sandy, S. Myers, B. Klein, N. Gautam, P. Ahirwar, Z.-B. Tian, T. Rotter, G. Balakrishnan, E. Plis and S. Krishna, "Gallium free type II InAs/InAsxSb1-x superlattice photodetectors," *Applied Physics Letters,* vol. 071111, no. 101, 2012.